Progress in Neurobiology 208 (2022) 102177

Contents lists available at ScienceDirect

Progress in Neurobiology

journal homepage: www.elsevier.com/locate/pneurobio

Original Research Article

The Celsr3-Kif2a axis directs neuronal migration in the postnatal brain

Janne Hakanen [a], Nicolas Parmentier [a], Leonie Sommacal [a,2], Dario Garcia-Sanchez [a], Mohamed Aittaleb [b], Didier Vertommen [c], Libing Zhou [d], Nuria Ruiz-Reig [a,1], Fadel Tissir [a,b,*,1]

[a] Université catholique de Louvain, Institute of Neuroscience, Developmental Neurobiology, Brussels, Belgium
[b] College of Health and Life Sciences, Hamad Bin Khalifa University, Doha, Qatar
[c] Université catholique de Louvain, de Duve Institute, Massprot Platform, Brussels, Belgium
[d] Guangdong-Hongkong-Macau Institute of CNS Regeneration, Ministry of Education CNS Regeneration Collaborative Joint Laboratory, Jinan University, Guangzhou, 510632, PR China

ARTICLE INFO

Keywords:
Postnatal neurogenesis
Tangential migration
Planar cell polarity
Cytoskeletal dynamics

ABSTRACT

The tangential migration of immature neurons in the postnatal brain involves consecutive migration cycles and depends on constant remodeling of the cell cytoskeleton, particularly in the leading process (LP). Despite the identification of several proteins with permissive and empowering functions, the mechanisms that specify the direction of migration remain largely unknown. Here, we report that planar cell polarity protein Celsr3 orients neuroblasts migration from the subventricular zone (SVZ) to olfactory bulb (OB). In *Celsr3*-forebrain conditional knockout mice, neuroblasts loose directionality and few can reach the OB. Celsr3-deficient neuroblasts exhibit aberrant branching of LP, de novo LP formation, and decreased growth rate of microtubules (MT). Mechanistically, we show that Celsr3 interacts physically with Kif2a, a MT depolymerizing protein and that conditional inactivation of *Kif2a* in the forebrain recapitulates the *Celsr3* knockout phenotype. Our findings provide evidence that Celsr3 and Kif2a cooperatively specify the directionality of neuroblasts tangential migration in the postnatal brain.

1. Introduction

Brain development involves extensive migration of neuroblasts over long distances to reach their final destinations. The majority of neuroblasts differentiate and migrate to their final positions during embryonic period in the mammalian brain (Lim and Alvarez-Buylla, 2016; Wichterle et al., 2001). However, neurogenesis and neuronal migration do persist in restricted areas in the postnatal/adult brain. Postnatally generated neuroblasts in the subventricular zone (SVZ) migrate through rostral migratory stream (RMS) into the olfactory bulbs (OB) where they differentiate into distinct subsets of interneurons and integrate into the preexisting olfactory circuitries (Alvarez-Buylla and Garcia-Verdugo, 2002; Batista-Brito et al., 2008; Khodosevich et al., 2013; Lledo et al., 2008; Lois et al., 1996; Whitman and Greer, 2007). Postnatally generated OB interneurons participate in processing olfactory inputs impacting odor learning, discrimination and memory (Alonso et al., 2012; Shimshek et al., 2005). Therefore, postnatal neurogenesis in the SVZ and migration of neuroblasts towards OB shape olfactory perception and animal behavior (Alonso et al., 2012; Forest et al., 2019). The tangential migration of neuroblasts in RMS is regulated by several extracellular and intracellular factors that modify the migratory behavior (Kaneko et al., 2017; Wichterle et al., 1997). Neuroblasts migrate in chains in close contact with glial cells and blood vessels. Therefore, cell-cell contacts and cell- extracellular matrix interactions are important permissive factors that facilitate neuroblasts migration. On the other hand, neuroblasts directionality and speed rely on proper progression of migratory cycle and branching (Belvindrah et al., 2017; Cooper, 2013; Kaneko et al., 2017; Marin et al., 2010; Nakamuta et al., 2017). The migratory cycle begins when neuroblasts extend their leading process (LP) to sample surrounding environment while the centrosome and soma remain stationary. This exploration phase is followed by LP stabilization and centrosome movement into the dilation which is formed into the base of LP. After centrosome movement, nucleus and soma migrate towards the centrosome in a process called somal translocation. The migratory cycle including LP extension, migration of the cell organelles and somal translocation is then repeated consecutively

* Corresponding author at: Avenue Mounier 73 Box B1.73.16, Belgium.
E-mail addresses: fadel.tissir@uclouvain.be, ftissir@hbku.edu.qa (F. Tissir).
[1] Equal contribution.
[2] Current address: INSERM, Neurocentre Magendie, U1215, 33000 Bordeaux, France; Université Bordeaux, Neurocentre Magendie, 33000 Bordeaux, France.

https://doi.org/10.1016/j.pneurobio.2021.102177
Received 23 May 2021; Received in revised form 12 August 2021; Accepted 20 September 2021
Available online 25 September 2021

during migration (Cooper, 2013; Schaar and McConnell, 2005; Tsai and Gleeson, 2005). MT dynamics has a major role in many processes during the migratory cycle, such as LP extension, migration of the cell organelles and somal translocation (Rivas and Hatten, 1995; Tsai and Gleeson, 2005). MT dynamics affect the initiation, frequency, length, and life-time of LP branches (Godin et al., 2012; Kappeler et al., 2006; Nakamuta et al., 2017; Sonego et al., 2015). Time-lapse imaging and genetic studies have started to unveil the role of intrinsic factors and molecules that have an impact on neuroblasts cytoskeleton dynamics (Belvindrah et al., 2017; Godin et al., 2012; Nakamuta et al., 2017). Yet, how migrating neuroblasts integrate intrinsic and extrinsic cues and elicit cytoskeletal changes for a proper migration remain still largely unknown.

Celsr3 (Cadherin, EGF-like, Laminin G-like, Seven pass, G-type Receptor 3) is an evolutionary conserved adhesion G protein-coupled receptor belonging to planar cell polarity (PCP) pathway (Goffinet and Tissir, 2017). Celsr3 acts by homo- and heterotypic interactions to coordinate intercellular polarity and support different developmental processes (Lindenmaier et al., 2019; Shima et al., 2007; Tissir and Goffinet, 2013). During the embryonic development, Celsr3 is involved in axon guidance (Tissir et al., 2005; Zhou et al., 2008), neural progenitor cell differentiation (Wang et al., 2016), neuronal migration (Qu et al., 2010; Ying et al., 2009), and ependymal ciliogenesis (Boutin et al., 2014; Tissir et al., 2010).

Here, we report that Celsr3 is highly expressed in the RMS at the peak of the postnatal neurogenesis. We combined genetic and molecular approaches with time-lapse imaging and found that Celsr3 plays a critical role during tangential migration of neuroblasts from SVZ to OB. Celsr3 interacts with Kif2a (kinesin superfamily protein 2a), a member of kinesin 13 gene family (Friel and Welburn, 2018) that, in addition to its motor function, triggers depolymerization of MTs in ATP dependent manner (Ogawa et al., 2017; Trofimova et al., 2018). Celsr3 and Kif2a cooperatively control migratory cycle and LP branching through cytoskeleton dynamics and determine directionality and speed of neuroblasts migration.

2. Material and methods

2.1. Animals

All animal procedures were approved by the animal ethics committee of the Université catholique de Louvain and carried out in compliance with European guidelines. Mouse lines used in this study were: *Celsr3*$^{f/f}$ (Tissir et al., 2005), *Kif2a*$^{f/f}$ (Fig. S2), *Foxg1-Cre* (Hebert and McConnell, 2000) and *Dlx5/6-cre-EGFP* (Stenman et al., 2003). For generation of conditional *Celsr3* and *Kif2a* knock-out mice (*Celsr3* cKO and *Kif2a* cKO), *FoxG1-Cre;Celsr3*$^{+/-}$ and *FoxG1-Cre;Kif2a*$^{+/-}$ males were crossed with *Celsr3*$^{f/f}$ and *Kif2a*$^{f/f}$ females, respectively. For time lapse imaging *FoxG1-Cre;Dlx5/6-Cre-EGFP;Celsr3*$^{+/-}$ and *FoxG1-Cre;Dlx5/6-Cre-EGFP;Kif2a*$^{+/-}$ males were crossed with *Celsr3*$^{f/f}$ and *Kif2a*$^{f/f}$ females to produce *Celsr3* and *Kif2a* knock-out mice in which Dlx5/6 derivatives express GFP (*Celsr3* cKO-EGFP and *Kif2a* cKO-EGFP).

2.2. Olfactory bulb (OB) measurement

OB length and width were measured from fresh P12 brains imaged with Leica stereo microscope (MDG41) equipped with Leica DFC450 camera. A total number of five mice were studied per genotype.

2.3. Immunoprecipitation and western blotting

All reagents were purchased from ThermoFisher Scientific, unless specified otherwise. E14.5 brains (WT) were collected and stored at −80 °C until use. Immunoprecipitation (IP) was performed on pools of eight brains homogenized with 0.8 ml of lysis buffer (Tris 15 mM pH 7.4, Glycerol 2%, Triton-X100 1%, Halt-protease and phosphatase inhibitor). For Kif2a-IP, Triton-X100 was eventually replaced by N-dodecyl-β-D-maltoside (DDM) or n-octyl-β-D-glucoside (N-OG) from the lysis buffer. Brain homogenates were incubated for 30 min at 4 °C on a tube rotator and insoluble materials were removed by centrifugation (20.000xg/10 min/4 °C). IPs were performed using the Pierce crosslink magnetic co-IP kit (Thermo Fisher scientific, 88855) following the manufacturer's instructions. Briefly 10 µg of guinea pig anti-Celsr3 antibodies (Lindenmaier et al., 2019) and normal guinea serum (Sigma, G9774 used as negative control); and rabbit polyclonal anti-Kif2a (Abcam, ab37005) and normal rabbit serum (Sigma, 12–370) were crosslinked on 25µl of Protein A/G magnetic beads. Antibodies-beads complexes resuspended with 300 µl of IP-buffer (IPB), were incubated 2 h at RT with 300 µl of brain extracts. The flowthrough was recovered, and the beads were washed with 500 µl of successively IPB, IPB + NaCl 500 mM, IPB. Protein complexes were eluted by incubating beads 8 min (RT) with 125 µl of acidic elution solution, (100 mM glycine−HCl, 100 mM citric acid, pH 3.0), 10 µl was evaluated by WB was and 115 µl for mass spectrometry (see below). For WB, only the elution fraction and the first two washes of IP (referred to in Fig. 4 as "E", "Wash", and "NaCl", respectively) were denatured in LDS-sample buffer + DTT 50 mM (overnight at 56 °C then 20 min at72 °C after DTT-renewal). Protein were separated on a Tris-acetate 3–8 % SDS-PAGE electrophoresis gradient-gel and transferred onto PVDF membrane. The membrane was blocked 1 h with nonfat milk 6% diluted in TBS + Tween 0.1 % and probed ON at 4 °C with Antibodies diluted in the same buffer (Celsr3 1:7500, Kif2a 1/8000). Secondary antibodies, anti-rabbit (Cell Signaling-7074, 1:20000), anti-guinea pig (Merck Millipore-AP108 P, 1:7500), were incubated 1 h at room temperature. The HRP-signal was detected on X-ray film using a mix of Supersignal reagent (Thermofisher scientific).

2.4. Mass spectrometry

For mass spectrometry, elution fractions (115 µl) of both Celsr3-IP and Control-IP (normal guinea pig serum) were first concentrated by Methanol/chloroform precipitation (Wessel and Flugge, 1984). Precipitates were solubilized in 35 µl of LDS sample buffer with DTT 50 mM ON at 4 °C, then 20 min at 42 °C and finally 20 min at 72 °C, after DTT renewal. Protein were separated by electrophoresis and gel was stained with colloidal Coomassie blue. The gel was divided in 4 slices *per* well, excised, in-gel digested with trypsin and analyzed by liquid chromatographic tandem mass spectrometry. Peptides were dissolved in solvent A (0.1 % TFA in 2% ACN), directly loaded onto reversed-phase pre-column (Acclaim PepMap 100, Thermo Scientific) and eluted in backflush mode. Peptide separation was performed using a reversed-phase analytical column (Acclaim PepMap RSLC, 0.075 × 250 mm,Thermo Scientific) with a linear gradient of 4 %–27.5 % solvent B (0.1 % formic acid in 98 % acetonitrile) for 100 min, 27.5 %–40 % solvent B for 10 min, 40 %–95 % solvent B for 1 min and holding at 95 % for the last 10 min at a constant flow rate of 300 nl/min on an EASY-nLC 1000 RSLC system couple to a LTQ XL (linear ion trap) from ThermoScientific equipped with a nanospray ESI source. The MS scan routine was set to analyze by MS/MS the 10 most intense ions of each full MS scan, dynamic exclusion was enabled to assure detection of co-eluting peptides. Protein identification was performed with Sequest HT. Specifically, peak lists were generated using extract-msn (ThermoScientific) within Proteome Discoverer 2.2. The resulting peak lists were searched using SequestHT against a target-decoy *Mus musculus* protein database (101 302 entries comprising forward and reversed sequences) obtained from Uniprot. The following parameters were used: trypsin was selected with proteolytic cleavage only after arginine and lysine, number of internal cleavage sites was set to 1, mass tolerance for precursors and fragment ions was 1.0 Da, considered dynamic modifications were +15.99 Da for oxidized methionine. Peptide matches were filtered using the q-value and Posterior Error Probability calculated by the Percolator algorithm ensuring an estimated false positive rate below 5%.

2.5. Immunohistochemistry

At postnatal day (P) 12, mice were perfused with phosphate-buffered saline, pH 7.4 (PBS), followed by 4% paraformaldehyde (PFA). The brains were dissected out and post-fixed in 4% PFA at 4 °C for overnight, cryoprotected in 10 %, 20 % and 30 % sucrose series in PBS at 4 °C, and cut in sagittal plan into 50 μm thick sections with a sliding microtome (Thermo Scientific™, HM 450). Sections were blocked for immunostaining 2 h in PBS containing 3% bovine serum albumin and 0.5 % Triton X-100, followed by incubation with primary antibody at 4 °C for overnight. Primary antibodies used were rabbit anti-doublecortin (1:400, Cell Signaling Technology Cat# 4604, RRID: AB_561007) and rabbit anti-Kif2a (1:1000, Abcam Cat# ab37005, RRID: AB_2296593). Secondary antibody used was anti-rabbit AlexaFluor568 (1:500, Thermo Fisher Scientific Cat# A10042, RRID: AB_2534017). The nuclei were visualized using DAPI (4′,6-diamidino-2-phenylindole, Sigma). Sections were collected onto coated glass slides (SuperFrostPlus, Thermo Scientific™) and mounted with Mowiol mounting medium (0.1 M Tris−HCl, pH 8.5, 25 % glycerol, 10 % Mowiol 4–88 Reagent, Calbiochem; and 2.5 % 1,4-diazabicyclo-[2.2.2]-octan, Sigma-Aldrich). They were imaged by laser scanning confocal microscope (Olympus Fluoview FV1000). Images were assembled using Fiji software (Schindelin et al., 2012), and imported into Adobe Photoshop 2019 for montage. Calculations of RMS width and cell numbers were performed in three distinct areas: proximal RMS (area size, 525 μm x 150 μm), middle/elbow of the RMS (area size, 400 μm x 150 μm), and distal RMS (area size 400 μm x 150 μm). These areas were imaged completely through sections with confocal microscopy using 5 μm sampling interval. Three optical slices per area, starting at the level of RMS widest point, were calculated to obtain corresponding slices and overlapping was avoided by calculating every second slice. Calculations were performed with ImageJ (Fiji) software. Spot counter plugin was used to automatically count for nuclei (settings, box 3, noise 100). Cell counter plugin was used to count doublecortin- and DAPI-cells. A total number of four mice were studied for *Celsr3* cKO and for littermate controls. Three mice were studied for *Kif2a* cKO and for littermate controls. All values are given as mean ± SEM. Student's *t*-test was performed for the statistical analysis.

2.6. Organotypic brain slice culture

Organotypic brain slice cultures were used for imaging neuroblast migration in RMS. At P12, mice were anesthetized and sacrificed. Dissected brains were immediately placed into ice cold artificial cerebrospinal fluid (aCSF; NaCl 125 mM, KCl 3 mM, $MgCl_2$ 1 mM, $CaCl_2$ 2 mM, NaH_2PO_4 1.25 mM, $NaHCO_3$ 25 mM, HEPES 25 mM, Glucose 10 mM) and cut into 150 μm thick sagittal slices with a vibratome (Leica VT1000S). Slices containing RMS were transferred into tissue culture insert (Picmorg50, Millicell®) within a glass-bottomed cell culture dish (627860, CELLview, Greiner bio-one) containing pre-warmed aCSF (+37 °C), and incubated for ~2 h at +37 °C in a 5% CO_2 before time lapse imaging.

2.7. Postnatal electroporation in vivo

Electroporation was performed mainly as described previously (Boutin et al., 2008). Briefly, P1–2 *Celsr3* cKO, *Kif2a* cKO and control mouse pups were anesthetized on ice ~3 min before injection. 2 μl of plasmid solution at concentration ~4 μg/μl were injected into the lateral ventricles using glass-pulled pipette connected to 2 μl Hamilton. Five 50-ms pulses of 90−100 V, with 850-ms interval were then delivered with tweezer electrodes positioned on each side of the pup's head. After electroporation, pups were reanimated on a +37 °C heating pad and returned to their mother. Co-electroporated plasmids were pCAG-PACT-mKO1-N1 plasmid (PACT domain of pericentrin-2 protein fused with a fluorescent protein mKO1), generous gift from Professor F. Matsuzaki (Riken Kobe Institute, Japan) to stain the centrosome, and Green Fluorescent Protein (GFP) eukaryotic expression vector based on the chicken beta-actin promoter and the CMV enhancer (pCX-EGFP-N1) was used to visualize electroporated cells. Brains were extracted one week after electroporation and placed into ice cold aCSF. Electroporated hemispheres were collected and cut with a vibratome into 150 μm thick sagittal slices. Slices containing fluorescently labeled neuroblasts along the RMS were transferred into a tissue culture insert (Picmorg50, Millicell®) placed in a glass-bottomed cell culture dish (PS, 35/10 mm, Gibco) containing prewarmed aCSF (+37 °C) and incubated for ~2 h at +37 °C in a 5% CO_2 incubator prior to time lapse imaging.

2.8. Time-lapse imaging and analysis

Time lapse imaging was performed with inverted Zeiss Axio Observer microscope equipped with environmental chamber (37 °C, 5% CO_2; Pecon) and Zeiss Axiocam 503 mono camera. Time lapses of organotypic and *in vivo* electroporated brain slices were taken using a 10x (NA = 0.45) objective (Zeiss). Images were captured every three minutes for 8−12 hours and each image was generated by compressing 4–6 z-stack images (6 μm interval) into a single frame. For neuroblasts speed and directionality, we tracked all *Dlx5/6-Cre-EGFP* positive neuroblasts which were visible in the vertical limb of RMS (RMS cross-section covering 400 μm in height, movie S2 and S10) for at least 6 h. Neuroblast tracking was performed manually with ImageJ plugin MtrackJ. A total number of 408 neuroblasts were tracked for *Celsr3* cKO-EGFP (at least 100 neuroblasts/mouse, n = 4) and 222 neuroblasts for littermate controls (at least 50 neuroblasts/mouse, n = 4). A total number of 727 neuroblasts were tracked for *Kif2a* cKO-EGFP (at least 100 neuroblasts/mouse, n = 4) and 224 neuroblasts for litter mate controls (at least 50 neuroblasts/mouse, n = 4). To distinguish stationary and migrating neuroblasts, we divided all tracked neuroblasts into bins according to the distance they had migrated during 6 h. Neuroblasts which had migrated over 90 μm/6 h (mean speed of 15 μm/h) were defined as moving neuroblasts and included in further analyses (*Celsr3* cKO-EGFP, n = 253 and control, n = 164 trajectories. *Kif2a* cKO-EGFP, n = 296 and control n = 172 trajectories). The collapsed optical stacks (Z-stacks, 24–36 micrometers of RMS) did not take in account the movement in 3D. Migrating neuroblasts moved vertically in relation to the microscope objective by changing their "depth" inside RMS. Thus, our results may underestimate slightly the migration speed and distance. Neuroblasts speed varied from slow to high while migrating in RMS. This variation of speed can be presented as oscillations to analyze temporal changes in neuroblasts speed. From these oscillations, we measured the mean frequency between maximum (peak) speeds and amplitude of oscillations per cell. For directionality, neuroblasts trajectories were transferred to begin from center point and directionality was quantified from the trajectory's endpoints (movie S3 and S12). A custom-made-open-source computer program, DiPer, was used to calculate neuroblasts directionality ratio (d/D) and last point directionality (Gorelik and Gautreau, 2014). All values are given as mean ± SEM, and Student's *t* test was performed for the statistical analyses. For migratory cycle analysis, we tracked LP, centrosome, and soma of the migrating neuroblasts for 6 h (Movie S5 and S14) and measured their velocity and distance relative to each other. The length and amplitude of the migratory cycle was quantified by measuring the distance between centrosome (stained with PACT-mKO1) and soma (GFP positive) over time. The distance between centrosome and soma is minimal at the beginning of the migratory cycle, and maximal when the centrosome moves forward in the leading process dilation. The variation of distance between the centrosome and soma was calculated for each time point to define the minimal and maximal distances. The amplitude of the migratory cycle was calculated as a mean difference between consecutive minimal and maximal distances over time per cell. The mean length of the migratory cycle was calculated as the number of maximal distances divided by measured time per cell. All values are given as mean ± SEM, and a Student's *t* test was used for the statistical analysis. For

nucleus-centrosome (N-C) coupling, we compared velocity of LP, centrosome, and soma relative to each other. A total number of 41 neuroblasts from four mice were studied for the *Celsr3* cKO and 41 neuroblasts from three mice for control mice. For *Kif2a* cKO, a total number of 38 neuroblasts from four mice were studied and 38 neuroblasts from three mice for control. Values were obtained by one-way ANOVA and Tukey post hoc test. For branching analysis, we quantified overall branching frequency as the number of new branches per hour. New branches were then divided into two categories according to the branching start point, (1) leading edge (LE) splitting, where the branching started from the growth cone-like structure located at the most distal part of LP, and (2) side branching from proximal LP or *de novo* LP formation from soma. For these two categories, we measured branching frequency per hour, maximum branch length and branch lifetime. A total number of 46 neuroblasts from five mice were studied for *Celsr3* cKO and 44 neuroblasts from four mice for control. For *Kif2a* cKO, a total number of 48 neuroblasts from five mice were studied and 44 neuroblasts from four mice for control. All values are given as mean ± SEM. Student's *t*-test was performed for the statistical analyses.

2.9. Astrocyte primary cultures

CD1 P2−4 mouse brains were dissected and cortices were isolated. Cortical cells were dissociated using papain, counted using a Bürker chamber, and plated in 75 cm^2 plastic flask at a density of ~10^4 cells/ml in astrocytes medium (DMEM high glucose, 10 % FBS, 1% Penicillin/streptomycin). Cells were kept in culture at least for one week and medium (Neurobasal™ -A Medium, minus phenol red (12349015, Gibco), B27™ supplement (17504−44,Gibco), L-glutamine 200 mM and Penicillin/streptomycin 1X) was changed every second day. When cells reached confluence, each type of glial cells was separated by two consecutives shaking: first, 180 rpm for 30 min to remove microglia, then 240 rpm for 6 h to remove oligodendrocytes. The remaining astrocytes were washed and detached in 5 ml of Trypsin/EDTA for 30 min. Finally, astrocytes were plated on 35 mm petri dishes at a density of ~3.10^4 cells/ml.

2.10. EB3 live imaging

RMS explants were prepared from 200 μm thick vibratome sections and placed into 35 mm petri dishes as floating cultures with neurobasal medium (Neurobasal™ -A Medium, minus phenol red (12349015, Gibco), B27™ supplement (17504−44,Gibco), L-glutamine 200 mM and Penicillin/streptomycin 1X). Lentiviral particles encoding EB3-RFP (LentiBrite™ EB3-RFP, 17-10222, Millipore) were added to cultures at a concentration of 3.3 × 10^6 infectious units/dish for 24 h. After transfection, explants were transferred on top of astrocyte monolayer culture and incubated for additional 24 h allowing neuroblasts to start migration (Fig. 4C, D). Time lapse imaging was then performed using Zeiss Axio Observer microscope equipped with environmental chamber (37 °C, 5% CO_2; Pecon), Zeiss Axiocam 503 mono camera and 63x (NA = 1.2) water immersion objective (Zeiss). Time lapse series were captured every 2 s for 3 min from EB-RFP positive neuroblasts that migrated out of the explant and exhibited a bipolar morphology. EB3-RFP comets movement was tracked from the base towards the tip of the leading process. All time lapses were then deconvoluted with Huygens professional software (automatic deconvolution using CMLE algorithm with S/N ratio 15). EB3 comets were tracked manually with ImageJ plugin MtrackJ and trajectories and velocities were quantified with Graphpad Prism 8. A total number of 21 cells were studied for *Celsr3* cKO and 10 cells for control from three independent explant cultures. For *Kif2a* cKO, 20 cells were studied and 10 cells for control from three independent explant cultures. Data are represented as Tukey`s box plots. All values are given as mean ± SEM. Student's *t*-test was performed for the statistical analysis.

2.11. MT assay

MTs/Tubulin *in vivo* Assay Kit (BK038, Cytoskeleton Inc.) was used according to the manufacturer instructions to determine relative amount of MT versus free tubulin content in forebrain. Forebrain samples weighing 0.05−0.1 *g* were collected from P12 mice and homogenized in 1 ml of 37 °C pre-warmed lysis buffer with a 25-gauge syringe needle. Cellular debris was removed from the samples by centrifugation of lysis buffer at 1500 × g for 5 min at 37 °C. After centrifugation, 500 μl of supernatant was transferred into a new tube and centrifuged at 100,000 × g at 37 °C for one hour to separate polymerized tubulins/MTs (pellet) from tubulin monomers (supernatant). Supernatant was collected into a new tube and pellet was re-suspended to equal amount of lysis buffer (500 μl) as supernatant. An equal amount of both polymerized tubulins/MTs (pellet) and tubulin monomers (supernatant) was loaded for each SDS/PAGE assay, followed by chemiluminescent Western blotting with sheep anti-tubulin antibody (1:5000, Cytoskeleton, Inc. Cat# ATN02, RRID:10708807) to detect both α- and β-tubulin. Quantification of Western blots was performed by using Gel analysis method in imageJ software. The relative αβ-tubulin level between polymerized tubulins/MTs (pellet) and tubulin monomers (supernatant) were achieved by dividing relative intensity of pellet with supernatant relative intensity. A total number of five forebrain samples were studied for *Celsr3* cKO and for littermate controls. All values are given as mean ± SEM. Student's *t*-test was performed for the statistical analysis.

3. Results

3.1. Neuroblasts accumulate in the vertical limb of RMS in Celsr3 cKO mice

While Celsr3 is expressed in virtually all postmitotic neurons during embryogenesis, its expression is sharply downregulated in the postnatal brain except in derivatives of adult neurogenesis, including cells in the hippocampal formation, SVZ and RMS (Fig. 1A) (Tissir et al., 2002; Tissir and Goffinet, 2006). Given the perinatal lethality of *Celsr3* null mice, and with aim to investigate the role of Celsr3 in postnatal neurogenesis, we produced and analyzed conditional knockout mice where Celsr3 is deleted in the forebrain (*Celsr$^{f/f}$;Foxg1-Cre*, hereafter referred to as *Celsr3* cKO). At postnatal day 12 (P12), *Celsr3* cKO forebrain and, especially, olfactory bulbs were smaller compared to controls from littermates (length: -17 ± 0.6 %, $P < 0.0001$; width: -11.6 ± 2.1 %, $P = 0.009$; Fig1. B–E and Fig. S1). We labeled the neuroblasts using doublecortin (DCX) immunostaining in brain sagittal sections at postnatal day (P) 12 when the production of olfactory interneurons peaks. Whereas the RMS had a uniform width from the SVZ to OB in control mice, the mutant RMS appeared irregular. It was thicker proximally and thinner distally compared to controls (Fig. 1F, G). To quantify these changes, we divided the RMS into 3 distinct areas and calculated the width, total number of cells, and number of neuroblasts in each area. In the proximal RMS (that is the beginning of the vertical arm; area a, a' in Fig. F, G), the width, total cell number, and number of neuroblasts were increased in *Celsr3* cKO compared to control littermates (width: +105.9 ± 12.3 %, $P < 0.0001$; total cell number of cells: +91.5 ± 9.3 %, $P < 0.0001$; and neuroblasts +85.5 ± 19.6 %, $P = 0.0025$; Fig. 1H). At elbow level (i.e. the transition between vertical and horizontal arms area b, b'), they rose by +56.7 ± 11.1 % ($P = 0.0002$); +42.7 ± 13.9 %, ($P = 0.0074$); and +50.3 ± 16.2 % ($P = 0.0019$) respectively (Fig. 1I). By contrast, in the distal RMS (area c, c'), they were all reduced in *Celsr3* cKO (width: -53.4 ± 2.6 %, $P < 0.000$; total cell number: -56.8 ± 1.6 %, $P < 0.0001$; and neuroblasts: -50.6 ± 5.9 %, $P = 0.0049$; Fig. 1J). Thus, a substantial proportion of neuroblasts failed to progress beyond the elbow and accumulated in the vertical arm of RMS in mutant mice, suggesting that Celsr3 is important for tangential migration of neuroblasts in the postnatal brain.

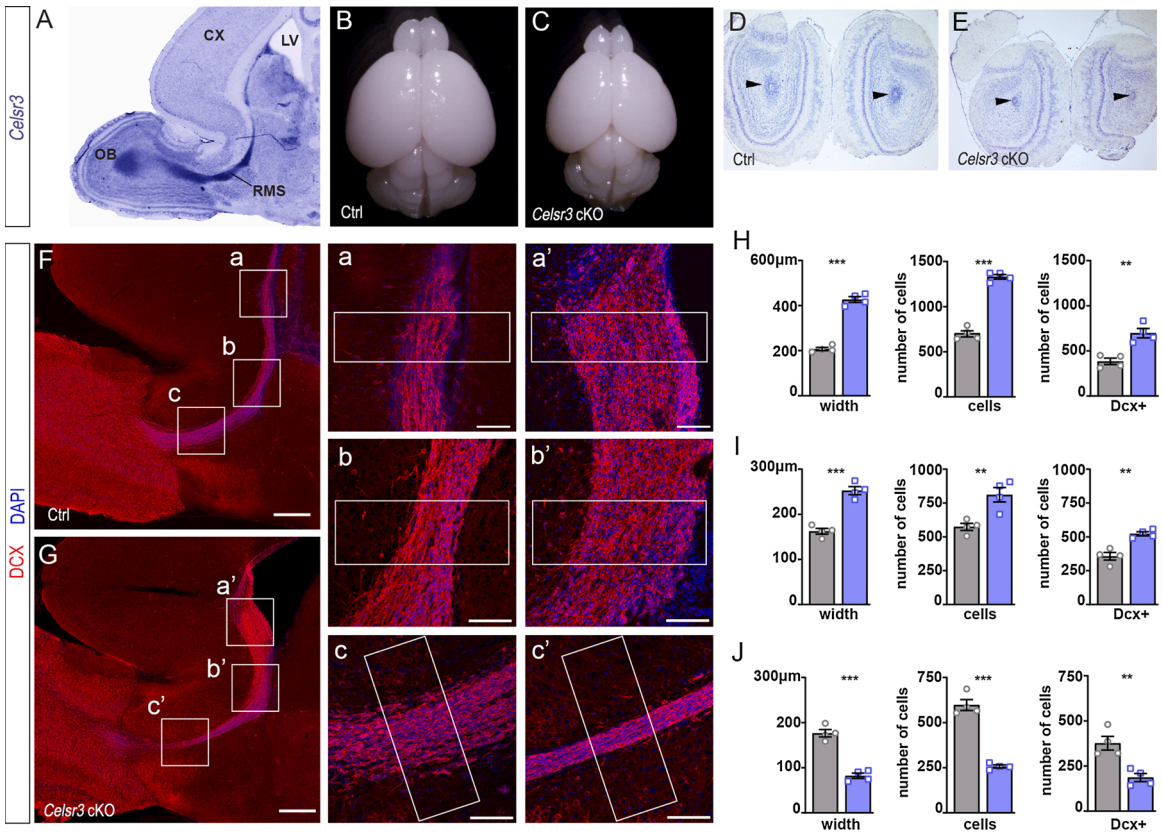

Fig. 1. Neuroblasts accumulate into the vertical RMS in *Celsr3* cKO mice. (A) *Celsr3* mRNA expression in the forebrain at P12. (B, C) P12 brains from control (B) and *Celsr3* cKO (C) mice. Nissl staining of control (D) and *Celsr3* cKO (E) mice olfactory bulb. (F, G) Composite images of sagittal brain sections from control (F) and *Celsr3* cKO (G) immunostained with anti-DCX (red) and DAPI (blue). White rectangles in F and G outlines enlarged areas in the proximal RMS (a, a'), elbow of the RMS (b,b') and distal RMS (c, c'). White boxes in the images (a, a'), (b, b') and (c, c') represents areas used for quantification of width, total number of cells and DCX positive cells. Scale bars, (A-D) 400 µm and (a-c') 100 µm. (H-J) Bar charts of width, total number of cells, and DCX positive cells in (a, a'), (b, b') and (c, c'), respectively. Control (gray color) n = 4 mice and *Celsr3* cKO (blue color) n = 4 mice. Data are represented as mean ± SEM. Values were obtained by unpaired Student's *t*-test; *: P < 0.05, **: P < 0.01, and ***: P < 0.001. OB, olfactory bulb. CX, cortex. LV, lateral ventricle. RMS, rostral migratory stream.

3.2. *Celsr3 specifies the direction and regulates velocity of migration*

Accumulation of neuroblasts in the proximal RMS could be due to impaired initiation of migration, prolonged stationary phase, or reduced speed of migration (Hakanen et al., 2011; Haumann et al., 2020; Nam et al., 2007; Turner and Sontheimer, 2014). To gain insights into the dynamics leading to accumulation of Celsr3-deficient neuroblasts in the vertical limb, we used time-lapse analysis. We crossed *Celsr3* cKO mice with Dlx5/6-Cre-EGFP mouse line to visualize a subpopulation of neuroblasts migrating from ventral telencephalon (Fig. 2A, movie S1) (Stenman et al., 2003). We measured the migration speed in acute brain slices by tracking neuroblasts present in the RMS vertical limb for a period of 6 h (Fig. 2B, Movie S2). Many Celsr3-deficient neuroblasts were motionless (Movie S1). To distinguish stationary and migrating cells, we segregated them into bins according to the distance they had migrated in 6 h and considered as "migrating" cells those that moved at least 90 µm. In *Celsr3* cKO-EGFP mice, 38 % of neuroblasts were stationary versus 26.1 % in control mice (Fig. 2C). The maximum migration length was 732 µm for Celsr3-deficient neuroblasts and 954 µm for control (Fig. 2C). After removal of stationary neuroblasts, the net displacement of neuroblasts was decreased in *Celsr3* cKO-EGFP mice compared to controls (-35.98 %, P < 0.0001, control = 421.6 ± 15.6 µm vs. *Celsr3* cKO-EGFP = 269.9 ± 9 µm, Fig. 2D). Consistent with these results, the migration speed of neuroblasts was reduced in *Celsr3* cKO-EGFP mice compared to controls (-38.99 %, P < 0.0001, control = 70.3 ± 2.6 µm/h, *Celsr3* cKO-EGFP = 45 ± 1.5 µm/h, Fig. 2E). Neuroblasts undergo saltatory movement (Belvindrah et al., 2017; Garcia--Gonzalez et al., 2017; Nam et al., 2007), we tested whether the saltatory migration pattern was preserved in Celsr3-deficient neuroblasts. We quantified neuroblasts frequency of peaks and amplitude of maximum velocities (Fig. 2F-H). Whereas the frequency of peaks was not affected (Fig. 2F, G), the amplitude was reduced in Celsr3 deficient neuroblasts compared to controls (-32.55 %, P < 0.0001, control = 114.9 ± 4.1 µm/h vs. *Celsr3* cKO-EGFP = 77.5 ± 2.3 µm/h Fig. 2F, H). We assessed the movement directionality by analyzing the trajectory of individual neuroblasts (movie S3, Fig. 2I-L). In control mice, 84.8 % of neuroblasts migrated toward OB, 6.1 % toward SVZ, and 9.1 % remained in the central ring (Fig. 2J left). In *Celsr3* cKO-EGFP mice, only 37.9 % migrated towards OB, 51.4 % toward SVZ and 10 % stayed inside the center (Fig. 2J right). Finally, we evaluated the directionality ratio (dD), which designates the deviation between the observed migration and optimal linear paths. Celsr3-deficient neuroblasts migration trajectory was significantly more curved compared to control neuroblasts (Fig. 2K). When the directionality ratio was measured from last point of the trajectories, Celsr3-deficient neuroblasts migration directionality deviated significantly from control neuroblasts (Fig. 2L; last point directionality, P = 0.006). These results show that Celsr3 is important for directionality and speed of neuroblasts migration but not for overall saltatory movement pattern.

3.3. *Defective migratory cycle and branching in Celsr3-deficient neuroblasts*

Neuroblasts migration is composed of consecutive migratory cycles that determine the migration speed. To scrutinize the migratory cycle, we labeled the neuroblast and centrosome by electroporating the pCX-

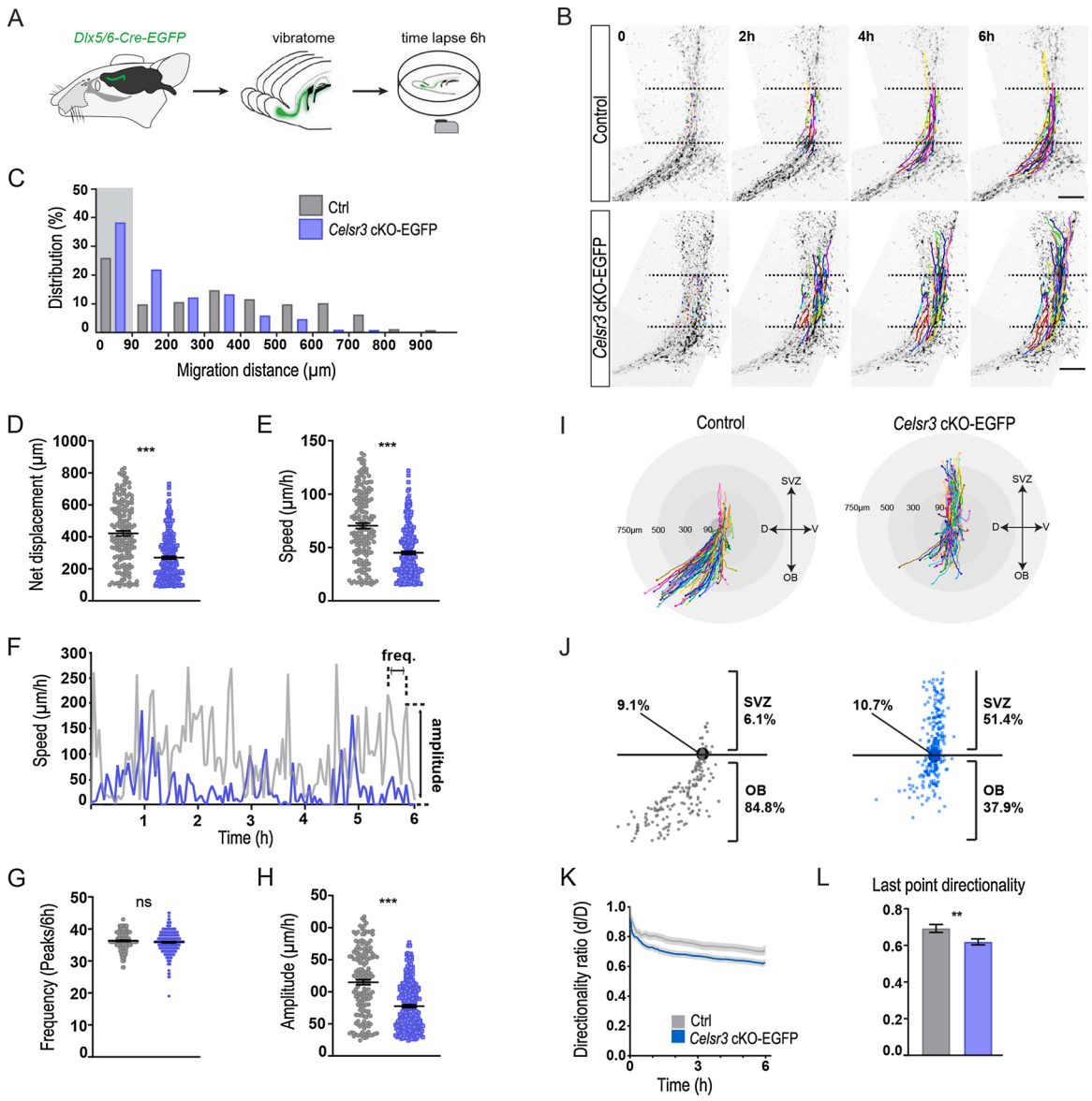

Fig. 2. Celsr3 regulates neuroblasts the direction and velocity of migration. (A) Scheme illustrating the time lapse imaging procedure. (B) Representative time lapse sequence illustrating tracking of neuroblasts in control and *Celsr3* cKO-EGFP mice. Neuroblasts which were visible between dashed lines (diameter, 400 µm) in the beginning of time lapse imaging were tracked for 6 h. Images are taken from video S2. Scale bars, 200 µm.
(C) Distribution of neuroblasts by migrated distance in control and *Celsr3* cKO-EGFP mice. Shaded area delineates stationary neuroblasts (0−90 µm) which were removed from further analysis. (D) Migrating neuroblasts net displacement in control and *Celsr3* cKO-EGFP mice. (E) Neuroblasts speed in control and *Celsr3* cKO-EGFP mice. (F) Representative graph illustrating temporal changes in migrating neuroblasts speed. (G) Frequency of neuroblasts peak speed in control and *Celsr3* cKO-EGFP mice. (H) Amplitude of neuroblasts speed in control and *Celsr3* cKO-EGFP mice. (I) Schematic illustration of neuroblasts migratory trajectories starting from center point. (J) the distribution of neuroblast directionality was quantified from trajectories endpoint. (J) In control mice (left), 84.8 % (139 trajectories) were directed towards the OB, 6.1 % (10 trajectories) towards the SVZ, and 9.1 % (15 trajectories) did not move out of the central ring (n = 164 trajectories, 4 mice). In *Celsr3* cKO-EGFP mice (right), 51.4 % (130 trajectories) moved towards the OB, 37.9 % (96 trajectories) towards the SVZ, and 10.7 % (27 trajectories) did not leave the center (n = 253 trajectories, 4 mice). (K) Neuroblasts directionality ratio (dD) analysis between control and *Celsr3* cKO-EGFP mice. Directionality ratio 1 denotes a straight migration trajectory from start to endpoint, and 0 a highly curved migration trajectory. Note that in *Celsr3* cKO-EGFP mice, neuroblast migration trajectory is closer to 0, suggesting a more curved neuroblast migration trajectory compared to control mice. (L) Last point directionality of control and *Celsr3* cKO-EGFP mice. For graphs (C–H and J–L), control (gray color) n = 164 cells from four animals and *Celsr3* cKO-EGFP (blue color) n = 253 cells from four animals. Data are represented as mean ± SEM. Values were obtained by unpaired Student's *t* test; ns = not significant, P < 0.01** and P < 0.001***. SVZ, subventricular zone. OB, olfactory bulb. D, dorsal. V, ventral.

EGFP and pCAG-PACT-mKO1-N1 plasmids into the lateral ventricle of neonates mice, and carried out time-lapse imaging on acute brain slices prepared 7 days after electroporation (Movie S4 and S5; Fig. 3A, B). Celsr3-deficient neuroblasts exhibited a longer LP (+22.22 %, P = 0.0048, control = 39.6 ± 1.7 µm vs. *Celsr3* cKO = 48.4 ± 2.4 µm; Fig. 3C, D), but the distance between centrosome and nucleus was reduced (-20 %, P = 0.0093, control = 8 ± 0.5 µm vs. *Celsr3* cKO vs. 6.4 ± 0.4 µm; Fig. 3E). This difference in centrosome positioning suggests that nucleus-centrosome (N-C) coupling could be defective in Celsr3 deficient neuroblasts, which may influence the somal translocation. To test this possibility, we compared velocities of LP, centrosome, and soma with respect to each other. Celsr3-deficient neuroblasts have reduced mean velocity for LP, centrosome and soma compared with control neuroblasts (LP velocity: -18.48 %, P = 0.0007, control = 108.2 ± 3.9

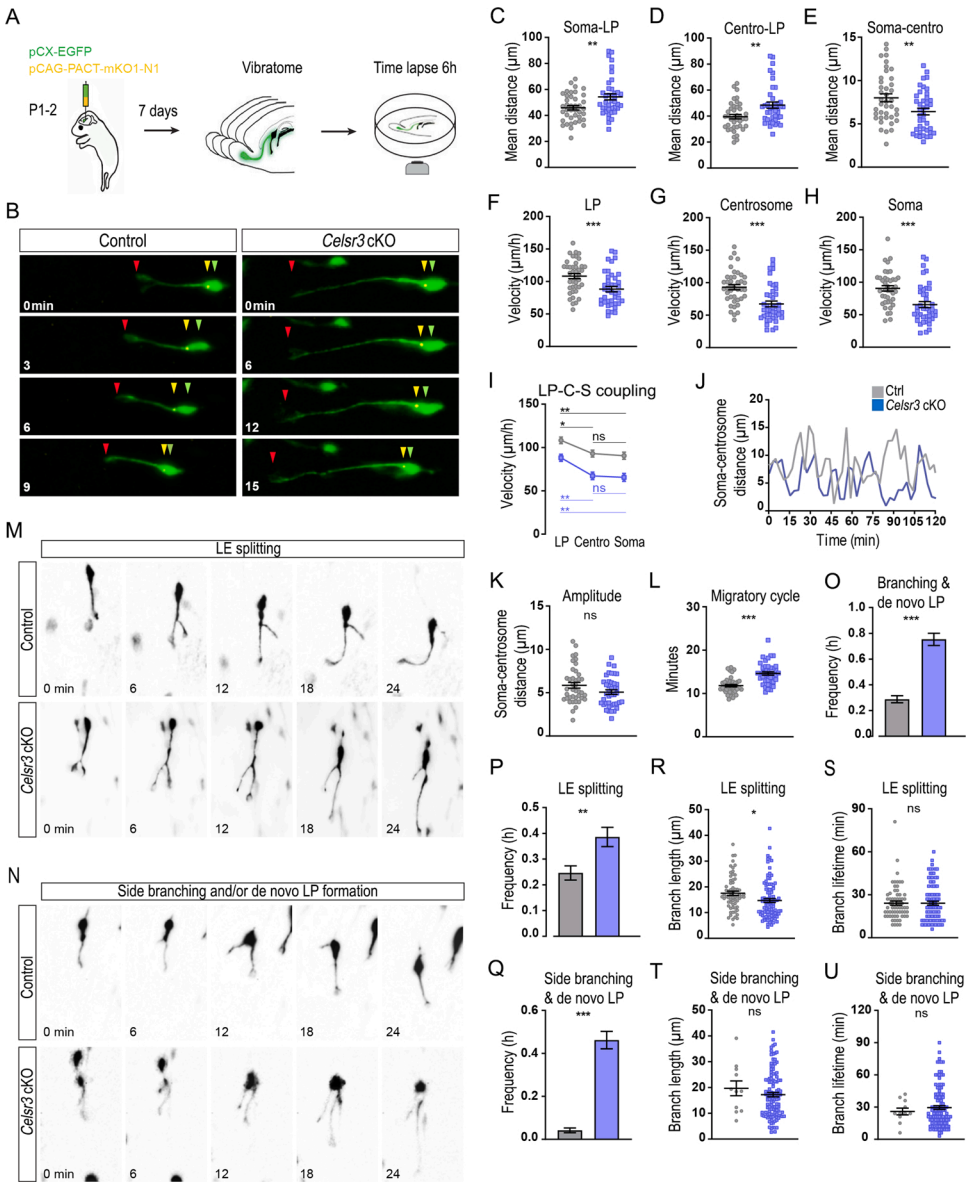

Fig. 3. Celsr3-deficient neuroblasts have longer migratory cycle and increased branching. (A) Scheme illustrating experimental procedure. Neonate control and *Celsr3* cKO mice were electroporated with pCX-EGFP and pCAG-PACT- mKO1-N1 plasmids to visualize neuroblasts morphology and centrosome position, respectively. Brain slices were analyzed 7 days after the electroporation with time lapse imaging. (B) Representative time lapse sequence emphasizing movement of the cell soma, centrosome, and LP during neuroblasts migration in RMS. Red arrowheads depict the end of LP, yellow arrowheads the position of the centrosome, and green arrowheads the position of cell soma. The timeline is shown in left down corner. (C-E) Quantification of the soma-end of LP distance, soma-centrosome distance, and centrosome-LP end distance. (F-H) Quantification of LP, centrosome and soma velocity. (I) Analysis of LP-C-S coupling. Note that LP-C-S coupling profiles are identical in control and *Celsr3* ^{cKO} mice. The quantifications were obtained by one-way ANOVA and Tukey post hoc tests. (J) Representative graph illustrating temporal changes in the distance between, soma, and centrosome in migrating neuroblasts. Control (gray) and *Celsr3* cKO (blue). (K) Quantification of mean amplitude of soma to centrosome distance during neuroblasts migration. (L) Quantification of migratory cycle duration. For graphs (C-L, n = 41 cells from three control mice (gray color), and 41 cells from four *Celsr3* cKO mice (blue color), Unpaired Student's *t* test). (M, N) Representative time lapse sequence illustrating neuroblasts branching. Branching category is indicated in the heading and mouse genotype on the side of the figure. The timeline is shown in left down corner. (O) Overall frequency of branching in control and *Celsr3* cKO mice (n = 44 cells from four control mice and 46 cells from five *Celsr3 cKO* mice). (P-U) Frequency, maximum branch length, and lifetime of leading edge (LE) splitting (P, R, and S, respectively); and of side branching (Q, T and U, respectively). Data are represented as mean ± SEM. Values were obtained by unpaired Student's *t* test; ns: not significant, *: P < 0.05, **: P < 0.01, and ***: P < 0.001.

µm/h vs. *Celsr3* cKO = 88.2 ± 4.1 µm/h; Fig. 3F. Centrosome velocity: -27.7 %, P < 0.0001, control = 93 ± 4 µm/h vs. *Celsr3* cKO = 67.2 ± 4.4 µm/h; Fig. 3G. Soma velocity: -27.5 %, P = 0.0002, control = 90.5 ± 4.2 µm/h vs. *Celsr3* cKO = 65.6 ± 4.7 µm/h; Fig. 3H). However, the relative connection between these three velocities was similar between control and mutant mice (Fig. 3I). In both cases, the neuroblasts LP velocity was significantly higher compared to the centrosome and soma velocities; but the centrosome and soma/nucleus velocities did not differ significantly from each other. These results suggest that the observed difference in the centrosome positioning is not due to defective N-C coupling. We also quantified the mean amplitude and duration of migratory cycle by measuring temporal variation in the soma-centrosome distance (Fig. 3J). The amplitude of soma-centrosome distance was not changed (P = 0.068, control = 5.9 ± 0.3 µm vs. *Celsr3* cKO 5.1 ± 0.3 µm; Fig. 3K). However, the mean duration of the migratory cycle was longer in Celsr3-deficient neuroblasts compared to controls (+23.73 %, P < 0.0001, control = 11.8 ± 0.3 min. vs. *Celsr3* cKO = 14.6 ± 0.4 min.; Fig. 3L). These results suggest that the movement range of the centrosome and soma is intact in Celsr3-deficient neuroblasts during the migratory cycle.

The extended migratory cycle is caused by uniform reduction of LP, centrosome, and soma velocities. A major factor in directing neuroblasts pathfinding is LP branching during migration (Cooper, 2013; Valiente and Martini, 2009). Thus, we analyzed LP branching from the time lapses (movies S6 and S7 and Fig. 3M, N). The overall branching frequency was much higher in Celsr3-deficient neuroblasts compared to controls (+158.62 %, P < 0.0001, control = 0.29 ± 0.03 branching events/hour vs. *Celsr3* cKO = 0.75 ± 0.05 branching events/hour; Fig. 3O). Branching normally occurs at the leading edge (Cooper, 2013). However, we observed branches emerging from different starting points (movies S6 and S7 and Fig. 3P, Q). Therefore, we divided the branching into two categories: (1) leading edge (LE) splitting, and (2) side branching from proximal LP or *de novo* LP formation from soma. In Celsr3-depleted neuroblasts, the frequency of both categories was increased (LE splitting +56 %, P = 0.0035, control = 0.25 ± 0.03 branching events/hour vs. *Celsr3* cKO = 0.39 ± 0.04; Fig. 3P. Side branching orde novo LP formation +1050 %, P < 0.0001, control = 0.04 ± 0.01 branching events/hour vs. *Celsr3* cKO = 0.46 ± 0.04 branching events/hour; Fig. 3Q). We also quantified the maximum length and

lifetime of the branches in both categories (Fig. 3R-U). In Celsr3-deficient neuroblasts, the length of branches was slightly decreased in LE splitting compared to control neuroblasts (-16 %, P = 0.0154, control = 17.5 ± 0.8 μm vs. *Celsr3* cKO 14.7 ± 0.8 μm; Fig. 3R). The maximum length of side branches and de novo LP, and the lifetime of both types were similar in the two genotypes (Fig. 3S-U). These results suggest that exuberant branching and prolonged migratory cycles cause the migration defects of Celsr3-deficient neuroblasts.

3.4. MT dynamics is impaired in Celsr3 cKO mice

Neuroblasts migration, directionality, migratory cycle and LP branching require constant rearrangement of the cell cytoskeleton (Kapitein and Hoogenraad, 2015). To investigate how Celsr3 may affect the cytoskeleton, we conducted a proteomic analysis on E.14.5 brain extracts. We identified 242 potential interactants (Supplementary Table 1). Kif2a, a Kinesin implicated in MT depolymerization and axonal transport, was selected for further investigations because i) it plays a role in radial migration (Homma et al., 2003), ii) it is expressed in the RMS during the peak of neuroblast migration, and iii) *Kif2a* KO and *Celsr3* KO mice have overlapping axonal phenotypes (Homma et al., 2003; Tissir et al., 2005). Celsr3-Kif2a interaction was confirmed by immunoprecipitation (IP) of endogenous Kif2a by anti-Celsr3 antibodies from embryonic day (E)14.5 brain extracts followed by western blotting (Fig. 4A). Inversely, anti- Kif2a antibodies immunoprecipitated Celsr3 (Fig. 4B) confirming the presence of the two proteins in the same complex. To explore the link between Celsr3 and MT dynamics in migrating Celsr3 neuroblasts, we transfected RMS explants with Lenti-Brite™ EB3-RFP fusion protein that binds to the MT plus end, and can be used to monitor the MT growth rate (Fig. 4C, D). Specifically, we tracked EB3-RFP fusion proteins (EB3 comets) movement in LP while neuroblasts migrated out of the RMS explants (Movie S8 and Fig. 4E). The movement of EB3 comets was slower in Celsr3-deficient neuroblasts than in controls. (-12.82 %, P = 0.0009, control = 0.39 ± 0.006 μm/sec vs. *Celsr3* cKO = 0.34 ± 0.009 μm/sec; Fig. 4F), indicating that the MT growth rate was reduced in the mutant tissue. To further analyze MT

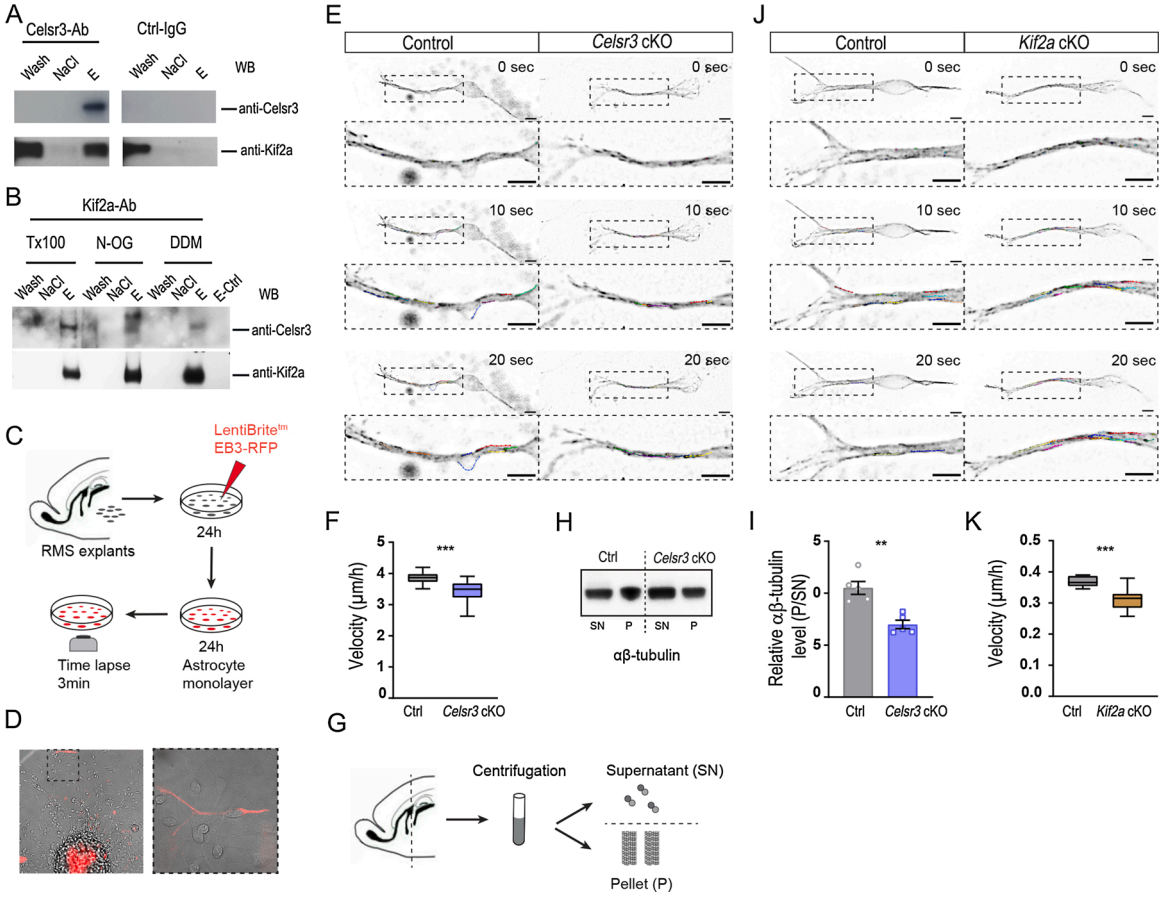

Fig. 4. MT dynamics is impaired in *Celsr3* cKO and *Kif2a* cKO neuroblasts. (A, B) Immunoprecipitation (IP) of Celsr3 and Kif2a from E14.5 brain extracts. Kif2a IP was performed with 3 different detergents: Triton X100 (Tx100), N-octylglucopyraoside (N-OG) and N-dodecyl maltoside (DDM). (C) Scheme illustrating the microtubule growth rate experiment. Explants were collected from RMS of P12 mice transfected with LentiBrite™ EB3-RFP and placed on top of the astrocyte monolayer. Time lapse imaging was performed in 2 s intervals for 3 min. (D) Representative image illustrating transfected explant and higher magnification (dashed square) showing the neuroblast imaged for time lapse (E) and Movie S8. (E) Representative time lapse sequence illustrating EB3-RFP comets tracking in control and *Celsr3* cKO neuroblasts. Dashed box in the upper panels presents the magnified area of the neuroblasts shown in dashed panels below. Time points 0 s, 10 s and 20 s. Scale bars 5 μm. (F) Quantification of EB3 comets velocity in control and *Celsr3* cKO neuroblasts. EB3 comets velocity data are represented as Tukey`s box plots, n = 10 cells (control, gray color) and 21 cells (*Celsr3* cKO cells, blue color) from three independent explant cultures per genotype. (G) Scheme illustrating microtubule the spin-down assay used to quantify polymerized microtubule (pellet fraction) versus non-polymerized (supernatant fraction) tubulin in control, and *Celsr3* cKO mice forebrain at P12. (H) Western blotting of control and *Celsr3* cKO mice supernatant (SN) and pellet (P) fractions with αβ-tubulin antibody. (I) Quantification of polymerized microtubule versus non-polymerized tubulin ratio between control and *Celsr3* cKO mice (n = 5 mice for each genotype). (J) Representative time lapse sequence illustrating EB3-RFP comets tracking in control and *Kif2a* cKO neuroblasts. Dashed box in the upper panels presents the magnified area of the neuroblasts shown in dashed panels below. Time points 0 s, 10 s and 20 s. Scale bars 5 μm. (K) Quantification of EB3 comets velocity in control and *Kif2a* cKO neuroblasts. Data are represented as Tukey`s box plots, n = 10 cells (control, gray) and 20 cells (*Kif2a* cKO cells, brown) from three independent explant cultures per genotype. Quantitative data are represented as mean ± SEM. Unpaired Student's *t* test; ns: not significant, *: P < 0.05, **: P < 0.01, and ***: P < 0.001.

dynamics, we performed a tubulin spin-down assay to quantify the ratio of polymerized MT and free (non-polymerized) tubulin. We used extracts of the RMS area and separated polymerized MT from non-polymerized tubulin by centrifugation (Fig. 4G). The ratio between polymerized MT and non-polymerized tubulin in Celsr3-deficient forebrain was smaller compared to control forebrains (-33.33 %, P = 0.0015, control = 1.05 ± 0.06 vs. *Celsr3* cKO = 0.7 ± 0.06; Fig. 4H, I). To test whether Kif2a could be involved in MT dynamics defects found in *Celsr3* cKO mice, we produced *Kif2a*-forebrain conditional knockout mice using the *Foxg1-Cre* line (*Kif2a* cKO) (Fig. S2 A–H). Like Celsr3, Kif2a depletion affected neuroblasts migration and MT dynamics (Movie S9, S10). EB3 comets movement in Kif2a-deficient neuroblasts was decreased compared to controls (-18.42 %, P < 0.0001, control = 0.38 ± 0.009 μm/sec vs. *Kif2a* cKO = 0.31 ± 0.007 μm/sec; Fig. 4J, K, Movie S10). These results suggest that Celsr3-deficiency affects the rate of MT growth/stability likely in Kif2a-dependent manner.

3.5. Deletion of *Kif2a* in the forebrain recapitulates the *Celsr3* cKO phenotype

In *Kif2a* cKO mice, the OB was markedly smaller than in controls at P12 (length: -23.5 ± 2%, P < 0.0001; width: -14.7 ± 1.4 %, P < 0.0001; (Fig. S1D, E and Fig. S2). We analyzed the distribution of neuroblasts using DCX staining (Fig. 5A, B), and detected a substantial accumulation of cells in the proximal RMS in *Kif2a* cKO mice (Fig. 5A, B a''-a''', C; width +158.1 ± 29.8 %, P = 0.0039; total number of cells: +145.1 ± 34.9 %, P = 0.0064; neuroblasts +147.6 ± 33.5 %, P = 0.0055). Accumulation of cells extended to the RMS elbow (Fig. 5A, B, b''-b''', D; width: +78.8 ± 13.9 %, P = 0.0028; total number of cells: +55.8 ± 13.1 %, P = 0.0045, neuroblasts: +61.2 ± 17.1 %, P = 0.0046; Fig). Hence, the distal RMS had shrunk and comprised less cells (Fig. 5A, B, c''-c''', E; width: -60.6 ± 6%, P = 0.0005; total number of cells: -60.1 ± 7.6 %, P = 0.002; neuroblasts: -57.7 ± 10.2 %, P = 0.0059). To assess whether these defects are due to impaired velocity and directionality, we performed time lapse imaging in *Kif2a* cKO; *Dlx5/6-Cre-EGFP* (*Kif2a* cKO-EGFP) mice (Fig. 6A; movie S11). 58.7 % of the neuroblasts were stationary in *Kif2a* cKO-EGFP versus 23.2 % in control mice (Fig. 6B). The maximum migration length was 564 μm for Kif2a-deficient and 774 μm for control neuroblasts (Fig. 6B). The net displacement of neuroblasts and the migration speed were significantly reduced in *Kif2a* cKO mutant mice compared to control mice (displacement: -47.45 %; P < 0.0001, control 380.2 ± 14.6 μm vs. *Kif2a* cKO-EGFP 199.8 ± 6.1 μm; Fig. 6C. Speed: -44.95 % P < 0.0001, control = 63.4 ± 2.4 μm/h vs. *Kif2a* cKO-EGFP 34.9 ± 1.1 μm/h; Fig. 6D). We analyzed the migratory pattern (Fig. 6E) and found that both the frequency of peaks and the mean amplitude of maximum velocity were reduced in *Kif2a* cKO (frequency: -4.1 %, P < 0.0001, control = 36.6 ± 0.2, *Kif2a* cKO-EGFP = 35.1 ± 0.2; Fig. 6F. Amplitude -45.16 %, P < 0.0001, control = 104.3 ± 3.9 μm/h, *Kif2a* cKO-EGFP = 57.2 ± 1.7 μm/h; Fig. 6G). The directionality was also affected as only 35 % of neuroblasts migrated toward OB in *Kif2a* cKO versus 82 % in control mice (Movie S12; Fig. 6H, I), and the migration end point significantly deviated from the normal path (Fig. 6J, K). To test whether the loss-of-function of Kif2a triggers similar modifications of migratory cycle and branching as those observed in *Celsr3* cKO mice, we electroporated pCX-EGFP and pCAG-PACT- mKO1-N1 expression vectors in lateral ventricles of newborn mice, and scrutinized neuroblast migration using time lapses in organotypic slices (Movie S13 and S14, Fig. 7A). Like in *Celsr3* cKO mice, LP was longer in Kif2a-depleted neuroblasts, and the distance between centrosome and soma was greatly extended compared to controls (LP length +53.55 %, P < 0.0001, control = 49.3 ± 1.4 μm vs. *Kif2a* cKO = 75.7 ± 2.7 μm; soma-centrosome distance +90.79 %, P < 0.0001, control = 7.6 ± 0.4 μm vs. *Kif2a* cKO = 14.5 ± 0.8 μm; Movie S14, Fig. 7B-D). The velocity of LP, centrosome and soma were decreased in Kif2a deficient neuroblasts compared to controls (LP velocity -20.96 %, P = 0.0002, control = 114.5 ± 3.8 μm/h vs. *Kif2a* cKO 90.5 ± 4.7 μm/h; centrosome velocity -36.55 %, P < 0.0001, control = 96.3 ± 4.6 μm/h vs. *Kif2a* cKO = 61.1 ± 4.3 μm/h; soma velocity -45.04 %, P < 0.0001, control = 95.7 ± 4.5 μm/h vs. *Kif2a* cKO = 52.6 ± 4.4 μm/h; Fig. 7E-G). Like in *Celsr3* cKO mice, the relative connection between these three velocities was identical between control and *Kif2a* cKO mice (Fig. 7H). We analyzed the migratory cycle (Fig. 7I) and observed no change in the cycle amplitude (Fig. 7J). However, the mean duration of the cycle was longer in *Kif2a* cKO (+47.27 %, P < 0.0001, control = 11 ± 0.3 min. vs. *Kif2a* cKO 16.2 ± 0.6

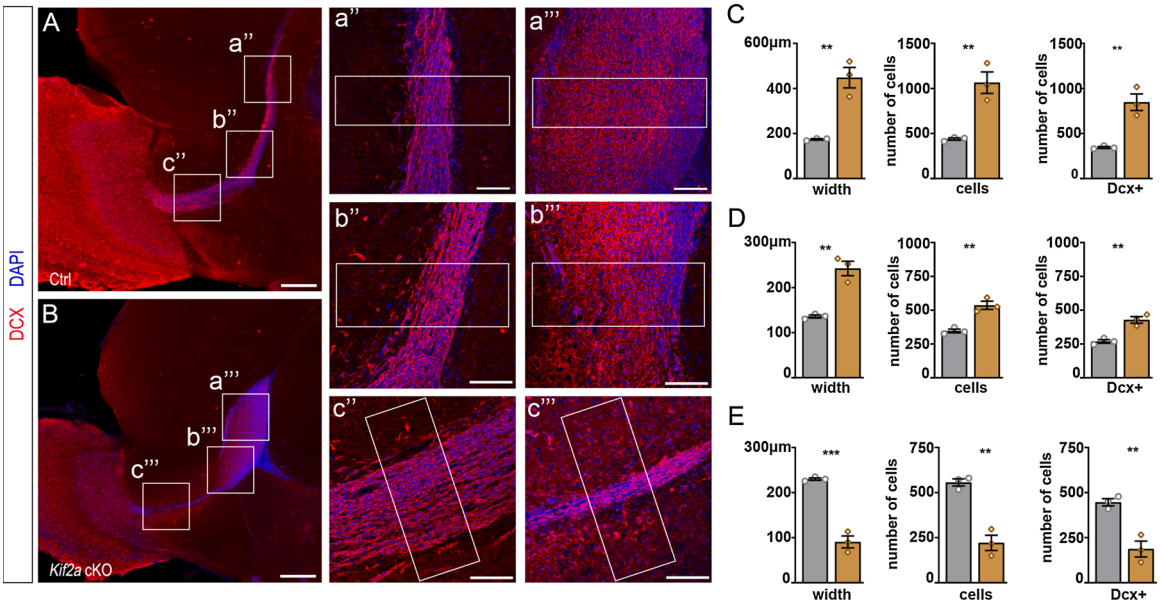

Fig. 5. Neuroblasts accumulate into the vertical RMS in *Kif2a* cKO mice.
(A, B) Immunostaining with anti-DCX (red) and DAPI (blue) of brain sagittal sections at P12 from control (A) and *Kif2a* cKO (B) mice. White boxes in (A, B left panels) outline enlarged areas in the corresponding right panels that were used for quantifications. Scale bars; 400 μm in (A, B) and 100 μm in (a-c'). (C–E) Quantification of the width, total number of cells and DCX positive cells in the proximal RMS (C; a: control, a': *Kif2a* cKO), elbow (D; b: control, b': *Kif2a* cKO) and distal RMS (E; c': control, c': *Kif2a* cKO). Control (gray color) and *Kif2a* cKO (brown color), n = 3 mice for each genotype. Data are represented as mean ± SEM, Unpaired Student's *t* test; *: P < 0.05, **: P < 0.01, and ***: P < 0.001.

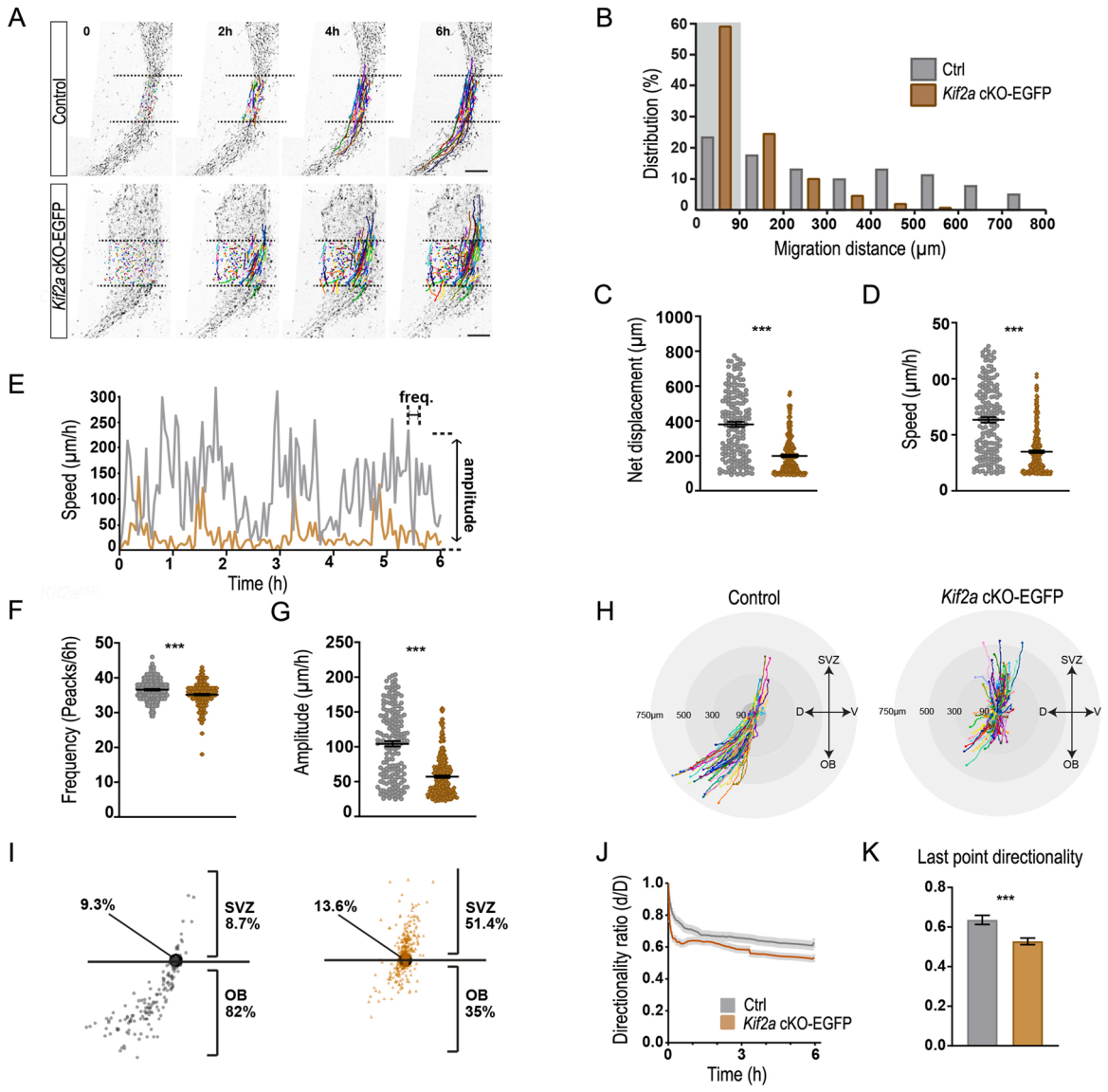

Fig. 6. Loss of Kif2a alters direction and velocity of migration.
(A) Representative time lapse sequence illustrating neuroblasts tracking in control and *Kif2a* cKO-EGFP mice. Neuroblasts which were comprised between the dashed lines (diameter, 400 μm) in the beginning of the time lapse imaging were tracked for 6 h. Images are taken from move S11. Scale bars, 200 μm. (B) Distribution of control and Kif2a-deficient neuroblasts by the migrated distance. The shaded area delineates the stationary neuroblasts (moved 0−90 μm) which were not considered for further analysis. (C) Net displacement in control and *Kif2a* cKO-EGFP mice. (D) Speed of migration in control and *Kif2a* cKO-EGFP mice. (E) Representative graph illustrating temporal changes in migrating neuroblasts speed in control (gray) and *Kif2a* cKO-EGFP (brown) mice. (F) Frequency of neuroblasts peak speed in control and *Kif2a* cKO-EGFP mice. (G) Amplitude of neuroblasts speed in control and Kif2a cKO-EGFP mice. (H) Schematic illustration of neuroblasts migratory trajectories starting from center point. . (I) Distribution of neuroblasts migratory direction was quantified from trajectories endpoint. In control mice (left), 82 % (141 trajectories) were directed towards the olfactory bulb, 8.7 % (15 trajectories) towards the SVZ and 9.3 % (16 trajectories) did not leave the central ring (n = 172 trajectories, 4 mice). In *Kif2a* cKO-EGFP mice (right), 51.4 % (105 trajectories) moved towards the olfactory bulb, 35 % (154 trajectories) towards the SVZ and 13.6 % (41 trajectories) did not move out of the central ring (n = 296 trajectories, 4 mice). (J) Directionality ratio (dD) analysis showed that the *Kif2a* cKO neuroblasts have more curved migration trajectory compared to the control mice. (K) Last point directionality of control and *Kif2a* cKO-EGFP. n = 172 control and 296 *Kif2a* cKO-EGFP cells from four animals for each genotype. Data are represented as mean ± SEM, Unpaired Student's *t* test; ***: P < 0.001.SVZ, subventricular zone. OB, olfactory bulb. D, dorsal. V, ventral.

min; Fig. 7K). We also quantified neuroblasts branching (movies S15 and S16; Fig. 7L, M). The frequency of branching was higher in Kif2a cKO compared to control neuroblasts (+161.54 %, P < 0.0001, control = 0.26 ± 0.03 branching events/hour vs. *Kif2a* cKO = 0.68 ± 0.06 branching events/hour; Fig. 7N), mainly because of a much greater side branching frequency (+940 %, P < 0.0001, control = 0.05 ± 0.02 branching events/hour vs. *Kif2a* cKO = 0.52 ± 0.06 branching events/hour; Fig. 7O, P). The maximum length and lifetime of the side branches were not changed (Fig. 7Q-T). Overall, these results show that the *Kif2a* cKO phenotype resembles that of *Celsr3* cKO mice, with accumulation of neuroblasts in the vertical limb of RMS, reduced migration velocity, prolonged migratory cycle, increased branching, and loss of directionally toward OB.

4. Discussion

Here, we report that Celsr3 and Kif2a regulate tangential migration in the postnatal brain. *Celsr3* cKO and *Kif2a* cKO mice exhibit an accumulation of neuroblasts in the vertical RMS, along with a decrease in their number in OB. Celsr3 and Kif2a-depleted cells have impaired

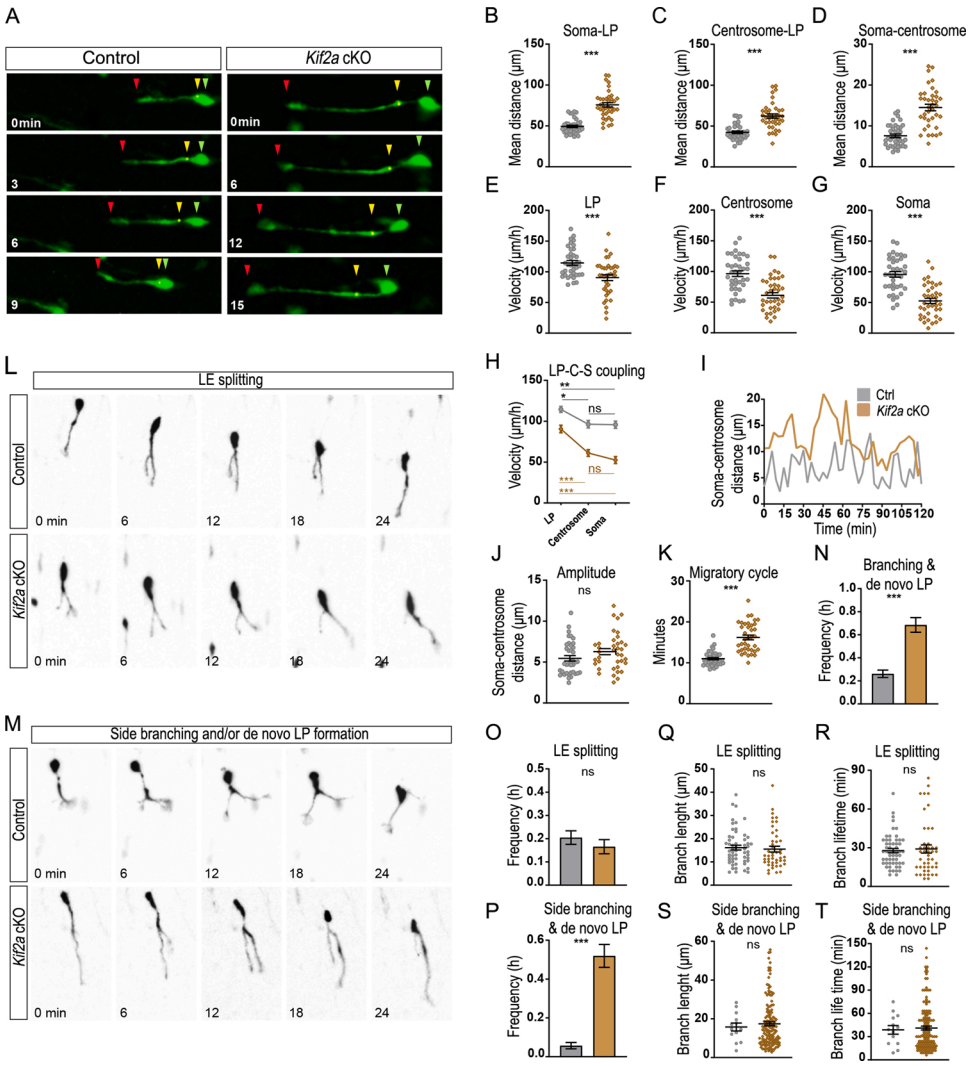

Fig. 7. Kif2a-deficient neuroblasts have prolonged migratory cycle and increased branching. (A) representative time lapse sequences illustrating movement of cell soma, centrosome, and LP during neuroblasts migration. pCX-EGFP and pCAG-PACT- mKO1-N1 signals are shown in green and yellow, respectively. The red arrowhead points to the tip of LP end, yellow arrowhead depicts the position of the centrosome, and green arrowhead the position of the cell soma. The timeline is shown in left down corner. (B-D) Quantification of the soma-LP, soma-centrosome, and centrosome-LP distance. (E-G) Quantification of the LP, centrosome, and soma velocity. (H) Analysis of LP-C-S coupling. Note that the LP-C-S coupling profiles are similar in the two genotypes. Analyses were performed using one-way ANOVA and Tukey post hoc test. (I) Representative graphs illustrating temporal changes in the distance between soma and centrosome in migrating neuroblasts. Control (gray) and *Kif2a* cKO (brown). (J) Quantification of mean amplitude of soma to centrosome distance. (K) Quantification of migratory cycle duration. For graphs (B-K), n = 38 cells from three control control mice (gray) and 38 cells from four *Kif2a* cKO mice (brown). (L, M) A representative time lapse sequence illustrating neuroblast branching during migration. Branching category is indicated in the heading and mouse genotype on the side of the figure. (N) Overall frequency of branching in control and *Kif2a* cKO mice. (O-T) Frequency, maximum branch length, and lifetime of leading edge splitting (O, Q, and R, respectively); and of side branching or de novo LP formation (P, S and T, respectively). n = 44 cells from four control mice and 48 cells from five *Kif2a* cKO mice. Data are represented as mean ± SEM; Unpaired Student's *t* test; ns: not significant, *: $P < 0.05$, **: $P < 0.01$, and ***: $P < 0.001$.

migration speed and directionality. The migratory cycle, branching of the leading process and MT dynamics are altered. Celsr3 interacts physically with Kif2a. This interaction, uncovered by Mass Spectrometry and confirmed by reciprocal Co-IPs, could be direct, or could involve other partners. The phenotype is, however, more severe in *Kif2a* cKO than that in *Celsr3* cKO, and minor differences between Celsr3 and Kif2a deficient neuroblasts were observed, suggesting that other proteins than Celsr3 act upstream of Kif2a during tangential migration of neuroblasts. To exit the neurogenic niche and migrate long distances towards OB, neuroblasts must integrate information from the extracellular environment and neighbor cells and transduce it into intracellular signals that trigger re-distribution of polarity proteins and remodeling of cell junctions and cytoskeleton. Therefore, transmembrane proteins at adherent junctions are key molecules in the process. For instance, N-cadherin mediates the adhesion of ependymocytes in the SVZ of adult mice and between neuroblasts while migrating towards the olfactory bulb (Fujikake et al., 2018; Porlan et al., 2014). Celsr cadherins are core component of the PCP signaling, which mediates cell adhesion and polarity and has been implicated in the tangential migration of facial branchiomotor neurons (Davey et al., 2016; Glasco et al., 2016, 2012; Qu et al., 2010; Vivancos et al., 2009; Yang et al., 2014). In this work, we show for the first time that the PCP protein Celsr3 is essential to centrosome positioning and LP dynamics. On the other hand, the intracellular polarity complexes underlying apicobasal polarity (e.g. Par3-Par6-aPKC, Crumbs-Pals1-Patj1, and Scribble-Lgl-Dlg) convey the extracellular signaling to the cytoskeleton (Raman et al., 2018), regulating different aspects of neuronal migration such as bipolar morphology, nuclear and centrosome movement, and LP dynamics (Hakanen et al., 2019; Jossin, 2020). Whether PCP acts upstream of or in parallel to apical basal polarity to remodel the cytoskeleton awaits further investigations. Note however that Scribble, a key regulator of apical basal polarity, has a documented role in PCP (Moreau et al., 2010; Sun et al., 2016) and might constitute the molecular link between the two pathways.

4.1. *Celsr3 and Kif2a direct neuronal migration*

Neuronal migration proceeds in a stereotypical manner and involves the repetition of migratory cycles. These events require persistent remodeling of cell cytoskeleton and is driven by actin- and MT-dependent forces (Bertipaglia et al., 2018; Etienne-Manneville, 2013; Kapitein and Hoogenraad, 2015). Our results show that neuroblasts lacking either Celsr3 or Kif2a have longer leading processes, suggesting that Celsr3-Kif2a axis regulates MT stability. Consistent with that, silencing Celsr3 in hippocampal neurons *in vitro* results in overgrowth of dendrites and axons (Shima et al., 2007). Similarly, axons and axon collaterals are longer in Kif2a depleted hippocampal neurons(Homma et al., 2003, 2018; Noda et al., 2012). It has been proposed that the centrosome serves as a central link between MT dependent forces generated from extending LP and the MT cage surrounding the nucleus to drive neuronal migration cycle (Higginbotham and Gleeson, 2007;

Rivas and Hatten, 1995; Tsai et al., 2007; Tsai and Gleeson, 2005; Xie et al., 2003). The MT network between the LP and centrosome forms a scaffold for dynein/kinesin reliant forces to move the centrosome forward into the dilation (Fructuoso et al., 2020; Tsai et al., 2007; Tsai and Gleeson, 2005). Furthermore, the network of MT that links the centrosome to nucleus mediates dynein/kinesin dependent forces to pull the latter towards the former (Shu et al., 2004). Therefore, dynein and its activators are major regulators of centrosome positioning during migratory cycle (Dantas et al., 2016; Luxton and Gundersen, 2011; Shu et al., 2004; Tsai and Gleeson, 2005). Dynein inhibition increases the distance between nucleus and centrosome (Luxton and Gundersen, 2011; Shu et al., 2004). Our results show that Celsr3 and Kif2a have opposite effects on positioning the centrosome and soma relative to each other. The centrosome to soma distance is narrowed in *Celsr3* cKO and stretched in *Kif2a* cKO compared to controls. These results suggest that Kif2a could affect dynein-mediated forces during somal translocation independently of Celsr3. Kif2a localizes to centrosome together with dynein activators and this localization is regulated by dynein pathway activator CDK5 (Chapman et al., 2019; Ding et al., 2019; Kodani et al., 2020). Dynein is also believed to target Kif2a into spindle poles in proliferating cells (Gaetz and Kapoor, 2004). Centrosome-soma uncoupling, i.e. abnormal relative distance between centrosome and soma also indicates impaired somal translocation (Bellion et al., 2005; Belvindrah et al., 2017; Nakamuta et al., 2017; Shu et al., 2004). Interestingly, Celsr3- and Kif2a-deficient neuroblasts show normal movement range of somal translocation suggesting that soma-centrosome coupling is preserved, despite the altered relative distance between the centrosome and soma. Celsr3- and Kif2a-deficient neuroblasts have reduced velocities of the leading process, centrosome, soma; decreased MT growth rate; and longer migratory cycle. Most likely, the reduced MT growth rate impairs LP extension, centrosome, and soma movement, and leads to longer migratory cycle. Similar protracted migratory cycle with reduced MT growth has been found in mutant with loss of MT associated protein p27 and Map1B (Godin et al., 2012; Takei et al., 2000; Tymanskyj et al., 2012). On the other hand, inhibiting dynein and its activators does not affect MT growth rate (Grabham et al., 2007; Kappeler et al., 2006; Moores et al., 2006; Pramparo et al., 2010; Tsai et al., 2007). Celsr3 modulates Kif2a function likely by affecting its depolymerizing activity. Kif2a-mediated MT depolymerization is phosphorylation-dependent (Ogawa et al., 2017). BDNF through its receptor TrkB and downstream effectors PAK1 and CDK5 kinases stimulates Kif2a phosphorylation (Ogawa et al., 2017). Lack of BDNF, TrkB, PAK1 and CDK5 have been shown to disrupt neuroblasts migration in RMS (Bagley and Belluscio, 2010; Hirota et al., 2007; Zhou et al., 2015). Whether the Celsr3 signal affects the phosphorylation of Kif2a awaits further investigations.

MT growth rate is decreased by either positive or negative changes in MT stability (Duellberg et al., 2016; Zanic et al., 2013). Kif2a is a MT destabilizer and its lack results in more stable MTs (Homma et al., 2003; Noda et al., 2012). Therefore, Celsr3-Kif2a interaction could regulate MT stability. Celsr3 deficient (forebrain) tissue also has less polymerized tubulin compared to control mice, suggesting that tubulin polymerization is impaired. Like Celsr3, ablation of the phosphoinositide-dependent protein kinase 1 (PDK1) reduces the amount of polymerized MT in brain. PDK1 knockout neurons have reduced amount of MAPs bound to the MTs, which is suggested to affect MT dynamics and thereby the amount of polymerized MT (Itoh et al., 2016). Intriguingly, despite the fact that Celsr3 is membrane bound protein, some tubulins, centrosomal- and microtubule-associated proteins (e.g. Tubulin gamma-1 chain, centrosomal protein of 164 kDa, centrosomal protein of 170 kDa, Kinesin family member 2A, Microtubule-associated protein 1B, Isoform 3 of Microtubule-associated protein 6, Dynein heavy chain 5, Dynactin subunit 1) were detected by MS as potential interactants of Celsr3 (supplementary Table S1).

4.2. LP branching facilitates pathfinding during neuronal migration

The branching occurs at the tip of LP and one of the branches is stabilized, defining the future direction of neuron movement (Cooper, 2013). The branching frequency negatively correlates with the migratory speed, so that the increased branching reduces the speed and vice-versa (Bear et al., 2002; Guerrier et al., 2009; Martinez-Molina et al., 2011). Many studies have indicated that MT assembly and disassembly rates determine both the extent and frequency of branching (Kapitein and Hoogenraad, 2015). Mutations in several MT associated proteins (e.g. DCX, Tuba1a, $p27^{kip1}$, Fascin, Drebrin E and Dock7) lead to aberrant branching and impaired migration (Belvindrah et al., 2017; Godin et al., 2012; Kappeler et al., 2006; Nakamuta et al., 2017; Sonego et al., 2013, 2015). Thus, branching is a key event during neuronal migration and links MT to both directionality and speed of movement. Leading edge splitting as well as side branching and de novo LP formation are markedly enhanced in Celsr3 and *Kif2a* cKO mice. In axons, interstitial side branching occurs by local destabilization of the MT and actin cytoskeleton (Brill et al., 2016; Luo, 2002). The impaired directionality and speed observed in neuroblasts lacking Celsr3 or Kif2a may result, at least partially, from increased branching frequency and compromised MT dynamics. The Celsr3-Kif2a signal through regulating MT dynamics is required for suppressing supernumerary branches and maintaining directionality of migrating neuroblasts in RMS.

Besides branching, neuroblasts form “chains” in RMS in contact with each other. These contacts are mediated by adhesion molecules and must be tightly regulated (Kaneko et al., 2017; Solecki, 2012). Adhesion molecules like integrins, PSA-NCAM and N-CAM are associated with the formation of neuroblast chains (Belvindrah et al., 2007; Chazal et al., 2000; Cremer et al., 1994; Mobley and McCarty, 2011). Disrupted chain formation is often reported with ectopic migration of neuroblasts into the surrounding tissues (Belvindrah et al., 2007; Sonego et al., 2013). We did not observe substantial ectopic migration of neuroblasts to the surrounding tissue both in *Celsr3* cKO and *Kif2a* cKO mice. However, many stationary neuroblasts were accumulating in the proximal RMS, thus causing its widening.

Altogether, our results suggest a model where the Celsr3-Kif2a axis regulates MT dynamics, thereby affecting the extension, branching and velocity of the leading process, as well as velocity of the centrosome and soma. This, in turn, regulates the duration of the migratory cycle, speed, and directionality of neuronal migration in the postnatal forebrain.

Declaration of Competing Interest

The authors report no declarations of interest.

Acknowledgements

We thank Isabelle Lambermont, and Clarisse Fouss for technical assistance. This work was supported by the following grants: FNRS PDR T00075.15, FNRS PDR T0236.20, FNRS-FWO EOS 30913351, Fondation Médicale Reine Elisabeth, and Fondation JED-Belgique. D G-S and N. R-R are Research Fellow and Postdoctoral Researcher at the Belgian Fund for Scientific Research (FNRS) respectively. FT is an Honorary Research Director FNRS.

Appendix A. The Peer Review Overview and Supplementary data

The Peer Review Overview and Supplementary data associated with this article can be found in the online version, at doi:https://doi.org/10.1016/j.pneurobio.2021.102177.

References

Alonso, M., Lepousez, G., Sebastien, W., Bardy, C., Gabellec, M.M., Torquet, N., Lledo, P. M., 2012. Activation of adult-born neurons facilitates learning and memory. Nat. Neurosci. 15, 897–904.

Alvarez-Buylla, A., Garcia-Verdugo, J.M., 2002. Neurogenesis in adult subventricular zone. J. Neurosci. 22, 629–634.

Bagley, J.A., Belluscio, L., 2010. Dynamic imaging reveals that brain-derived neurotrophic factor can independently regulate motility and direction of neuroblasts within the rostral migratory stream. Neuroscience 169, 1449–1461.

Batista-Brito, R., Close, J., Machold, R., Fishell, G., 2008. The distinct temporal origins of olfactory bulb interneuron subtypes. J. Neurosci. 28, 3966–3975.

Bear, J.E., Svitkina, T.M., Krause, M., Schafer, D.A., Loureiro, J.J., Strasser, G.A., Maly, I. V., Chaga, O.Y., Cooper, J.A., Borisy, G.G., Gertler, F.B., 2002. Antagonism between Ena/VASP proteins and actin filament capping regulates fibroblast motility. Cell 109, 509–521.

Bellion, A., Baudoin, J.P., Alvarez, C., Bornens, M., Metin, C., 2005. Nucleokinesis in tangentially migrating neurons comprises two alternating phases: forward migration of the Golgi/centrosome associated with centrosome splitting and myosin contraction at the rear. J. Neurosci. 25, 5691–5699.

Belvindrah, R., Hankel, S., Walker, J., Patton, B.L., Muller, U., 2007. Beta1 integrins control the formation of cell chains in the adult rostral migratory stream. J. Neurosci. 27, 2704–2717.

Belvindrah, R., Natarajan, K., Shabajee, P., Bruel-Jungerman, E., Bernard, J., Goutierre, M., Moutkine, I., Jaglin, X.H., Savariradjane, M., Irinopoulou, T., Poncer, J.C., Janke, C., Francis, F., 2017. Mutation of the alpha-tubulin Tuba1a leads to straighter microtubules and perturbs neuronal migration. J. Cell Biol. 216, 2443–2461.

Bertipaglia, C., Goncalves, J.C., Vallee, R.B., 2018. Nuclear migration in mammalian brain development. Semin. Cell Dev. Biol. 82, 57–66.

Boutin, C., Diestel, S., Desoeuvre, A., Tiveron, M.C., Cremer, H., 2008. Efficient in vivo electroporation of the postnatal rodent forebrain. PLoS One 3, e1883.

Boutin, C., Labedan, P., Dimidschstein, J., Richard, F., Cremer, H., Andre, P., Yang, Y., Montcouquiol, M., Goffinet, A.M., Tissir, F., 2014. A dual role for planar cell polarity genes in ciliated cells. Proc. Natl. Acad. Sci U S A 111, E3129–3138.

Brill, M.S., Kleele, T., Ruschkies, L., Wang, M., Marahori, N.A., Reuter, M.S., Hausrat, T. J., Weigand, E., Fisher, M., Ahles, A., Engelhardt, S., Bishop, D.L., Kneussel, M., Misgeld, T., 2016. Branch-specific microtubule destabilization mediates axon branch loss during neuromuscular synapse elimination. Neuron 92, 845–856.

Chapman, D.E., Reddy, B.J.N., Huy, B., Bovyn, M.J., Cruz, S.J.S., Al-Shammari, Z.M., Han, H., Wang, W., Smith, D.S., Gross, S.P., 2019. Regulation of in vivo dynein force production by CDK5 and 14-3-3epsilon and KIAA0528. Nat. Commun. 10, 228.

Chazal, G., Durbec, P., Jankovski, A., Rougon, G., Cremer, H., 2000. Consequences of neural cell adhesion molecule deficiency on cell migration in the rostral migratory stream of the mouse. J. Neurosci. 20, 1446–1457.

Cooper, J.A., 2013. Cell biology in neuroscience: mechanisms of cell migration in the nervous system. J. Cell Biol. 202, 725–734.

Cremer, H., Lange, R., Christoph, A., Plomann, M., Vopper, G., Roes, J., Brown, R., Baldwin, S., Kraemer, P., Scheff, S., et al., 1994. Inactivation of the N-CAM gene in mice results in size reduction of the olfactory bulb and deficits in spatial learning. Nature 367, 455–459.

Dantas, T.J., Carabalona, A., Hu, D.J., Vallee, R.B., 2016. Emerging roles for motor proteins in progenitor cell behavior and neuronal migration during brain development. Cytoskeleton (Hoboken) 73, 566–576.

Davey, C.F., Mathewson, A.W., Moens, C.B., 2016. PCP signaling between migrating neurons and their planar-polarized neuroepithelial environment controls filopodial dynamics and directional migration. PLoS Genet. 12, e1005934.

Ding, W., Wu, Q., Sun, L., Pan, N.C., Wang, X., 2019. Cenpj regulates cilia disassembly and neurogenesis in the developing mouse cortex. J. Neurosci. 39, 1994–2010.

Duellberg, C., Cade, N.I., Holmes, D., Surrey, T., 2016. The size of the EB cap determines instantaneous microtubule stability. Elife 5.

Etienne-Manneville, S., 2013. Microtubules in cell migration. Annu. Rev. Cell Dev. Biol. 29, 471–499.

Forest, J., Moreno, M., Cavelius, M., Chalencon, L., Ziessel, A., Sacquet, J., Richard, M., Didier, A., Mandairon, N., 2019. Short-term availability of adult-born neurons for memory encoding. Nat. Commun. 10, 5609.

Friel, C.T., Welburn, J.P., 2018. Parts list for a microtubule depolymerising kinesin. Biochem. Soc. Trans. 46, 1665–1672.

Fructuoso, M., Legrand, M., Mousson, A., Steffan, T., Vauchelles, R., De Mey, J., Sick, E., Ronde, P., Dujardin, D., 2020. FAK regulates dynein localisation and cell polarity in migrating mouse fibroblasts. Biol. Cell 112, 53–72.

Fujikake, K., Sawada, M., Hikita, T., Seto, Y., Kaneko, N., Herranz-Perez, V., Dohi, N., Homma, N., Osaga, S., Yanagawa, Y., Akaike, T., Garcia-Verdugo, J.M., Hattori, M., Sobue, K., Sawamoto, K., 2018. Detachment of chain-forming neuroblasts by fyn-mediated control of cell-cell adhesion in the postnatal brain. J. Neurosci. 38, 4598–4609.

Gaetz, J., Kapoor, T.M., 2004. Dynein/dynactin regulate metaphase spindle length by targeting depolymerizing activities to spindle poles. J. Cell Biol. 166, 465–471.

Garcia-Gonzalez, D., Khodosevich, K., Watanabe, Y., Rollenhagen, A., Lubke, J.H.R., Monyer, H., 2017. Serotonergic projections govern postnatal neuroblast migration. Neuron 94 (534–549), e539.

Glasco, D.M., Sittaramane, V., Bryant, W., Fritzsch, B., Sawant, A., Paudyal, A., Stewart, M., Andre, P., Cadete Vilhais-Neto, G., Yang, Y., Song, M.R., Murdoch, J.N., Chandrasekhar, A., 2012. The mouse Wnt/PCP protein Vangl2 is necessary for migration of facial branchiomotor neurons, and functions independently of Dishevelled. Dev Biol 369, 211–222.

Glasco, D.M., Pike, W., Qu, Y., Reustle, L., Misra, K., Di Bonito, M., Studer, M., Fritzsch, B., Goffinet, A.M., Tissir, F., Chandrasekhar, A., 2016. The atypical cadherin Celsr1 functions non-cell autonomously to block rostral migration of facial branchiomotor neurons in mice. Dev Biol 417, 40–49.

Godin, J.D., Thomas, N., Laguesse, S., Malinouskaya, L., Close, P., Malaise, O., Purnelle, A., Raineteau, O., Campbell, K., Fero, M., Moonen, G., Malgrange, B., Chariot, A., Metin, C., Besson, A., Nguyen, L., 2012. p27(Kip1) is a microtubule-associated protein that promotes microtubule polymerization during neuron migration. Dev. Cell 23, 729–744.

Goffinet, A.M., Tissir, F., 2017. Seven pass cadherins CELSR1-3. Semin. Cell Dev. Biol. 69, 102–110.

Gorelik, R., Gautreau, A., 2014. Quantitative and unbiased analysis of directional persistence in cell migration. Nat. Protoc. 9, 1931–1943.

Grabham, P.W., Seale, G.E., Bennecib, M., Goldberg, D.J., Vallee, R.B., 2007. Cytoplasmic dynein and LIS1 are required for microtubule advance during growth cone remodeling and fast axonal outgrowth. J. Neurosci. 27, 5823–5834.

Guerrier, S., Coutinho-Budd, J., Sassa, T., Gresset, A., Jordan, N.V., Chen, K., Jin, W.L., Frost, A., Polleux, F., 2009. The F-BAR domain of srGAP2 induces membrane protrusions required for neuronal migration and morphogenesis. Cell 138, 990–1004.

Hakanen, J., Duprat, S., Salminen, M., 2011. Netrin1 is required for neural and glial precursor migrations into the olfactory bulb. Dev Biol 355, 101–114.

Hakanen, J., Ruiz-Reig, N., Tissir, F., 2019. Linking cell polarity to cortical development and malformations. Front. Cell. Neurosci. 13, 244.

Haumann, I., Sturm, M.A., Anstotz, M., Rune, G.M., 2020. GPER1 signaling initiates migration of female V-SVZ-Derived cells. iScience 23, 101077.

Hebert, J.M., McConnell, S.K., 2000. Targeting of cre to the Foxg1 (BF-1) locus mediates loxP recombination in the telencephalon and other developing head structures. Dev Biol 222, 296–306.

Higginbotham, H.R., Gleeson, J.G., 2007. The centrosome in neuronal development. Trends Neurosci. 30, 276–283.

Hirota, Y., Ohshima, T., Kaneko, N., Ikeda, M., Iwasato, T., Kulkarni, A.B., Mikoshiba, K., Okano, H., Sawamoto, K., 2007. Cyclin-dependent kinase 5 is required for control of neuroblast migration in the postnatal subventricular zone. J. Neurosci. 27, 12829–12838.

Homma, N., Takei, Y., Tanaka, Y., Nakata, T., Terada, S., Kikkawa, M., Noda, Y., Hirokawa, N., 2003. Kinesin superfamily protein 2A (KIF2A) functions in suppression of collateral branch extension. Cell 114, 229–239.

Homma, N., Zhou, R., Naseer, M.I., Chaudhary, A.G., Al-Qahtani, M.H., Hirokawa, N., 2018. KIF2A regulates the development of dentate granule cells and postnatal hippocampal wiring. Elife 7.

Itoh, Y., Higuchi, M., Oishi, K., Kishi, Y., Okazaki, T., Sakai, H., Miyata, T., Nakajima, K., Gotoh, Y., 2016. PDK1-Akt pathway regulates radial neuronal migration and microtubules in the developing mouse neocortex. Proc. Natl. Acad. Sci. U.S.A 113, E2955–2964.

Jossin, Y., 2020. Molecular mechanisms of cell polarity in a range of model systems and in migrating neurons. Mol. Cell. Neurosci. 106, 103503.

Kaneko, N., Sawada, M., Sawamoto, K., 2017. Mechanisms of neuronal migration in the adult brain. J. Neurochem. 141, 835–847.

Kapitein, L.C., Hoogenraad, C.C., 2015. Building the neuronal microtubule cytoskeleton. Neuron 87, 492–506.

Kappeler, C., Saillour, Y., Baudoin, J.P., Tuy, F.P., Alvarez, C., Houbron, C., Gaspar, P., Hamard, G., Chelly, J., Metin, C., Francis, F., 2006. Branching and nucleokinesis defects in migrating interneurons derived from doublecortin knockout mice. Hum. Mol. Genet. 15, 1387–1400.

Khodosevich, K., Lazarini, F., von Engelhardt, J., Kaneko, H., Lledo, P.M., Monyer, H., 2013. Connective tissue growth factor regulates interneuron survival and information processing in the olfactory bulb. Neuron 79, 1136–1151.

Kodani, A., Kenny, C., Lai, A., Gonzalez, D.M., Stronge, E., Sejourne, G.M., Isacco, L., Partlow, J.N., O'Donnell, A., McWalter, K., Byrne, A.B., Barkovich, A.J., Yang, E., Hill, R.S., Gawlinski, P., Wiszniewski, W., Cohen, J.S., Fatemi, S.A., Baranano, K.W., Sahin, M., Vossler, D.G., Yuskaitis, C.J., Walsh, C.A., 2020. Posterior neocortex-specific regulation of neuronal migration by CEP85L identifies maternal centriole-dependent activation of CDK5. Neuron 106 (246–255), e246.

Lim, D.A., Alvarez-Buylla, A., 2016. The adult ventricular-subventricular zone (V-SVZ) and olfactory bulb (OB) neurogenesis. Cold Spring Harb. Perspect. Biol. 8.

Lindenmaier, L.B., Parmentier, N., Guo, C., Tissir, F., Wright, K.M., 2019. Dystroglycan is a scaffold for extracellular axon guidance decisions. Elife 8.

Lledo, P.M., Merkle, F.T., Alvarez-Buylla, A., 2008. Origin and function of olfactory bulb interneuron diversity. Trends Neurosci. 31, 392–400.

Lois, C., Garcia-Verdugo, J.M., Alvarez-Buylla, A., 1996. Chain migration of neuronal precursors. Science 271, 978–981.

Luo, L., 2002. Actin cytoskeleton regulation in neuronal morphogenesis and structural plasticity. Annu. Rev. Cell Dev. Biol. 18, 601–635.

Luxton, G.W., Gundersen, G.G., 2011. Orientation and function of the nuclear-centrosomal axis during cell migration. Curr. Opin. Cell Biol. 23, 579–588.

Marin, O., Valiente, M., Ge, X., Tsai, L.H., 2010. Guiding neuronal cell migrations. Cold Spring Harb. Perspect. Biol. 2, a001834.

Martinez-Molina, N., Kim, Y., Hockberger, P., Szele, F.G., 2011. Rostral migratory stream neuroblasts turn and change directions in stereotypic patterns. Cell Adh. Migr. 5, 83–95.

Mobley, A.K., McCarty, J.H., 2011. beta8 integrin is essential for neuroblast migration in the rostral migratory stream. Glia 59, 1579–1587.

Moores, C.A., Perderiset, M., Kappeler, C., Kain, S., Drummond, D., Perkins, S.J., Chelly, J., Cross, R., Houdusse, A., Francis, F., 2006. Distinct roles of doublecortin modulating the microtubule cytoskeleton. EMBO J. 25, 4448–4457.

Moreau, M.M., Piguel, N., Papouin, T., Koehl, M., Durand, C.M., Rubio, M.E., Loll, F., Richard, E.M., Mazzocco, C., Racca, C., Oliet, S.H., Abrous, D.N., Montcouquiol, M., Sans, N., 2010. The planar polarity protein Scribble1 is essential for neuronal plasticity and brain function. J. Neurosci. 30, 9738–9752.
Nakamuta, S., Yang, Y.T., Wang, C.L., Gallo, N.B., Yu, J.R., Tai, Y., Van Aelst, L., 2017. Dual role for DOCK7 in tangential migration of interneuron precursors in the postnatal forebrain. J. Cell Biol. 216, 4313–4330.
Nam, S.C., Kim, Y., Dryanovski, D., Walker, A., Goings, G., Woolfrey, K., Kang, S.S., Chu, C., Chenn, A., Erdelyi, F., Szabo, G., Hockberger, P., Szele, F.G., 2007. Dynamic features of postnatal subventricular zone cell motility: a two-photon time-lapse study. J. Comp. Neurol. 505, 190–208.
Noda, Y., Niwa, S., Homma, N., Fukuda, H., Imajo-Ohmi, S., Hirokawa, N., 2012. Phosphatidylinositol 4-phosphate 5-kinase alpha (PIPKalpha) regulates neuronal microtubule depolymerase kinesin, KIF2A and suppresses elongation of axon branches. Proc. Natl. Acad. Sci. U.S.A 109, 1725–1730.
Ogawa, T., Saijo, S., Shimizu, N., Jiang, X., Hirokawa, N., 2017. Mechanism of catalytic microtubule depolymerization via KIF2-Tubulin transitional conformation. Cell Rep. 20, 2626–2638.
Porlan, E., Marti-Prado, B., Morante-Redolat, J.M., Consiglio, A., Delgado, A.C., Kypta, R., Lopez-Otin, C., Kirstein, M., Farinas, I., 2014. MT5-MMP regulates adult neural stem cell functional quiescence through the cleavage of N-cadherin. Nat. Cell Biol. 16, 629–638.
Pramparo, T., Youn, Y.H., Yingling, J., Hirotsune, S., Wynshaw-Boris, A., 2010. Novel embryonic neuronal migration and proliferation defects in Dcx mutant mice are exacerbated by Lis1 reduction. J. Neurosci. 30, 3002–3012.
Qu, Y., Glasco, D.M., Zhou, L., Sawant, A., Ravni, A., Fritzsch, B., Damrau, C., Murdoch, J.N., Evans, S., Pfaff, S.L., Formstone, C., Goffinet, A.M., Chandrasekhar, A., Tissir, F., 2010. Atypical cadherins Celsr1-3 differentially regulate migration of facial branchiomotor neurons in mice. J. Neurosci. 30, 9392–9401.
Raman, R., Pinto, C.S., Sonawane, M., 2018. Polarized organization of the cytoskeleton: regulation by cell polarity proteins. J. Mol. Biol. 430, 3565–3584.
Rivas, R.J., Hatten, M.E., 1995. Motility and cytoskeletal organization of migrating cerebellar granule neurons. J. Neurosci. 15, 981–989.
Schaar, B.T., McConnell, S.K., 2005. Cytoskeletal coordination during neuronal migration. Proc. Natl. Acad. Sci. U.S.A 102, 13652–13657.
Schindelin, J., Arganda-Carreras, I., Frise, E., Kaynig, V., Longair, M., Pietzsch, T., Preibisch, S., Rueden, C., Saalfeld, S., Schmid, B., Tinevez, J.Y., White, D.J., Hartenstein, V., Eliceiri, K., Tomancak, P., Cardona, A., 2012. Fiji: an open-source platform for biological-image analysis. Nat. Methods 9, 676–682.
Shima, Y., Kawaguchi, S.Y., Kosaka, K., Nakayama, M., Hoshino, M., Nabeshima, Y., Hirano, T., Uemura, T., 2007. Opposing roles in neurite growth control by two seven-pass transmembrane cadherins. Nat. Neurosci. 10, 963–969.
Shimshek, D.R., Bus, T., Kim, J., Mihaljevic, A., Mack, V., Seeburg, P.H., Sprengel, R., Schaefer, A.T., 2005. Enhanced odor discrimination and impaired olfactory memory by spatially controlled switch of AMPA receptors. PLoS Biol. 3, e354.
Shu, T., Ayala, R., Nguyen, M.D., Xie, Z., Gleeson, J.G., Tsai, L.H., 2004. Ndel1 operates in a common pathway with LIS1 and cytoplasmic dynein to regulate cortical neuronal positioning. Neuron 44, 263–277.
Solecki, D.J., 2012. Sticky situations: recent advances in control of cell adhesion during neuronal migration. Curr. Opin. Neurobiol. 22, 791–798.
Sonego, M., Gajendra, S., Parsons, M., Ma, Y., Hobbs, C., Zentar, M.P., Williams, G., Machesky, L.M., Doherty, P., Lalli, G., 2013. Fascin regulates the migration of subventricular zone-derived neuroblasts in the postnatal brain. J. Neurosci. 33, 12171–12185.
Sonego, M., Oberoi, M., Stoddart, J., Gajendra, S., Hendricusdottir, R., Oozeer, F., Worth, D.C., Hobbs, C., Eickholt, B.J., Gordon-Weeks, P.R., Doherty, P., Lalli, G., 2015. Drebrin regulates neuroblast migration in the postnatal mammalian brain. PLoS One 10, e0126478.
Stenman, J., Toresson, H., Campbell, K., 2003. Identification of two distinct progenitor populations in the lateral ganglionic eminence: implications for striatal and olfactory bulb neurogenesis. J. Neurosci. 23, 167–174.
Sun, S.D., Purdy, A.M., Walsh, G.S., 2016. Planar cell polarity genes Frizzled3a, Vangl2, and Scribble are required for spinal commissural axon guidance. BMC Neurosci. 17, 83.
Takei, Y., Teng, J., Harada, A., Hirokawa, N., 2000. Defects in axonal elongation and neuronal migration in mice with disrupted tau and map1b genes. J. Cell Biol. 150, 989–1000.
Tissir, F., Goffinet, A.M., 2006. Expression of planar cell polarity genes during development of the mouse CNS. Eur. J. Neurosci. 23, 597–607.
Tissir, F., Goffinet, A.M., 2013. Shaping the nervous system: role of the core planar cell polarity genes. Nat. Rev. Neurosci. 14, 525–535.
Tissir, F., De-Backer, O., Goffinet, A.M., Lambert de Rouvroit, C., 2002. Developmental expression profiles of Celsr (Flamingo) genes in the mouse. Mech. Dev. 112, 157–160.
Tissir, F., Bar, I., Jossin, Y., De Backer, O., Goffinet, A.M., 2005. Protocadherin Celsr3 is crucial in axonal tract development. Nat. Neurosci. 8, 451–457.
Tissir, F., Qu, Y., Montcouquiol, M., Zhou, L., Komatsu, K., Shi, D., Fujimori, T., Labeau, J., Tyteca, D., Courtoy, P., Poumay, Y., Uemura, T., Goffinet, A.M., 2010. Lack of cadherins Celsr2 and Celsr3 impairs ependymal ciliogenesis, leading to fatal hydrocephalus. Nat. Neurosci. 13, 700–707.
Trofimova, D., Paydar, M., Zara, A., Talje, L., Kwok, B.H., Allingham, J.S., 2018. Ternary complex of Kif2A-bound tandem tubulin heterodimers represents a kinesin-13-mediated microtubule depolymerization reaction intermediate. Nat. Commun. 9, 2628.
Tsai, L.H., Gleeson, J.G., 2005. Nucleokinesis in neuronal migration. Neuron 46, 383–388.
Tsai, J.W., Bremner, K.H., Vallee, R.B., 2007. Dual subcellular roles for LIS1 and dynein in radial neuronal migration in live brain tissue. Nat. Neurosci. 10, 970–979.
Turner, K.L., Sontheimer, H., 2014. KCa3.1 modulates neuroblast migration along the rostral migratory stream (RMS) in vivo. Cereb. Cortex 24, 2388–2400.
Tymanskyj, S.R., Scales, T.M., Gordon-Weeks, P.R., 2012. MAP1B enhances microtubule assembly rates and axon extension rates in developing neurons. Mol. Cell. Neurosci. 49, 110–119.
Valiente, M., Martini, F.J., 2009. Migration of cortical interneurons relies on branched leading process dynamics. Cell Adh. Migr. 3, 278–280.
Vivancos, V., Chen, P., Spassky, N., Qian, D., Dabdoub, A., Kelley, M., Studer, M., Guthrie, S., 2009. Wnt activity guides facial branchiomotor neuron migration, and involves the PCP pathway and JNK and ROCK kinases. Neural Dev. 4, 7.
Wang, W., Jossin, Y., Chai, G., Lien, W.H., Tissir, F., Goffinet, A.M., 2016. Feedback regulation of apical progenitor fate by immature neurons through Wnt7-Celsr3-Fzd3 signalling. Nat. Commun. 7, 10936.
Wessel, D., Flugge, U.I., 1984. A method for the quantitative recovery of protein in dilute solution in the presence of detergents and lipids. Anal. Biochem. 138, 141–143.
Whitman, M.C., Greer, C.A., 2007. Synaptic integration of adult-generated olfactory bulb granule cells: basal axodendritic centrifugal input precedes apical dendrodendritic local circuits. J. Neurosci. 27, 9951–9961.
Wichterle, H., Garcia-Verdugo, J.M., Alvarez-Buylla, A., 1997. Direct evidence for homotypic, glia-independent neuronal migration. Neuron 18, 779–791.
Wichterle, H., Turnbull, D.H., Nery, S., Fishell, G., Alvarez-Buylla, A., 2001. In utero fate mapping reveals distinct migratory pathways and fates of neurons born in the mammalian basal forebrain. Development 128, 3759–3771.
Xie, Z., Sanada, K., Samuels, B.A., Shih, H., Tsai, L.-H., 2003. Serine 732 phosphorylation of FAK by Cdk5 is important for microtubule organization, nuclear movement, and neuronal migration. Cell 114, 469–482.
Yang, T., Bassuk, A.G., Stricker, S., Fritzsch, B., 2014. Prickle1 is necessary for the caudal migration of murine facial branchiomotor neurons. Cell Tissue Res. 357, 549–561.
Ying, G., Wu, S., Hou, R., Huang, W., Capecchi, M.R., Wu, Q., 2009. The protocadherin gene Celsr3 is required for interneuron migration in the mouse forebrain. Mol. Cell. Biol. 29, 3045–3061.
Zanic, M., Widlund, P.O., Hyman, A.A., Howard, J., 2013. Synergy between XMAP215 and EB1 increases microtubule growth rates to physiological levels. Nat. Cell Biol. 15, 688–693.
Zhou, L., Bar, I., Achouri, Y., Campbell, K., De Backer, O., Hebert, J.M., Jones, K., Kessaris, N., de Rouvroit, C.L., O'Leary, D., Richardson, W.D., Goffinet, A.M., Tissir, F., 2008. Early forebrain wiring: genetic dissection using conditional Celsr3 mutant mice. Science 320, 946–949.
Zhou, Y., Oudin, M.J., Gajendra, S., Sonego, M., Falenta, K., Williams, G., Lalli, G., Doherty, P., 2015. Regional effects of endocannabinoid, BDNF and FGF receptor signalling on neuroblast motility and guidance along the rostral migratory stream. Mol. Cell. Neurosci. 64, 32–43.